NTNU – Trondheim
Norwegian University of
Science and Technology

Hardness and Microstructure for Ge-Containing Al-Mg-Si-Cu alloys

Amund Fredrik Utne

Master of Science in Physics and Mathematics
Submission date: June 2012
Supervisor: Randi Holmestad, IFY

Norwegian University of Science and Technology
Department of Physics

Abstract

Four different Al-Mg-Si-Cu-Ge alloys with 0.002–0.037 at.% germanium were heat treated to the T6 condition and over-aged at 250°C for up to 100 hours. The hardness was tested during the over-ageing and there was a quick decrease in hardness from the start of the over-ageing. There was little difference in the hardness of the four alloys, however, there seemed to be a negative correlation between hardness and Ge-content. The alloy with 0.007 at.% Ge-content showed the greatest hardness, but there could be an error in the alloy composition. The two alloys with the most and least Ge-content were studied using a transmission electron microscope (TEM) after 24 and 100 hours of over-ageing, and the microstructure was analysed from the TEM images. No large difference in their microstructure was observed. The precipitates in the alloy with the least Ge-content were studied after 100 hours at 250°C in a scanning transmission electron microscope (STEM). The primary precipitates found were Q′ (and possibly Q), and some disordered Q′ precipitates. Energy-dispersive X-ray spectroscopy (EDX) showed no germanium in any of the precipitates.

Sammendrag

Fire forskjellige Al-Mg-Si-Cu-Ge legeringer med 0.002–0.037 at.% germanium ble varmebehandlet til T6 tilstanden og overeldret ved 250°C i opptil 100 timer. Hardheten ble testet i løpet av overeldringen og det var en rask reduksjon i hardhet fra starten av overeldringen. Det var liten forskjell i hardheten til de fire legeringene, men det så ut som det var en negativ korrelasjon mellom hardhet og germaniumsinnhold. Legeringen med 0.007 at.% germanium hadde den høyeste hardheten, men det er mulig at det er en feil med legeringssammensetningen. De to legeringene med mest og minst germanium ble studert i et transmisjonselektronmikroskop (TEM) etter 24 og 100 timer på 250°C, og mikrostrukturen ble analysert på basis av TEM bildene. Ingen stor forskjell i mikrostruktur ble observert. Kimene i legeringen med minst germanium ble studert etter 100 timer på 250°C i et Scanning transmisjonselektronmikroskop (STEM). De fleste kimene som ble funnet var Q′ (og muligens Q), og noen uordnede Q′ kim. Røntgen spektroskopi (EDX) viste ikke noe germanium i noen av kimene.

Preface

This report is my master thesis that was completed in the 10th semester of my 5 year Master of Technology, (Fysikk og Matematikk, siv. ing.) at the Norwegian University of Science and Technology (NTNU) during the spring of 2012.

I would like to thank my supervisor Professor Randi Holmestad for great supervising, feedback and enthusiasm, Calin D. Marioara from SINTEF for guidance, help with the TEM and getting the STEM images, Sigurd Wenner for a MATLAB script that made the microstructure analysis much easier and my sister Ane Aïda Utne for spell-checking. Finally a big thanks to everybody at the TEM Gemeni Center for being so nice and helpful people.

Amund F. Utne
June 14, 2012, Trondheim

Contents

Chapter 1

Introduction

Aluminium is the most abundant metal on the planet and around 8% of the weight of the Earth's crust consists of aluminium. However, it is a very reactive element and it is rarely found in its pure form, as it is primarily bound with oxygen or silicon.

Bauxite is the main source of aluminium for metal production. It is a combination of minerals containing various aluminium oxides and is defined by consisting of 40-60% alumina (Al_2O_3). Aluminium oxides are very stable and breaking them up requires a great amount of energy.

Aluminium has a wide range of properties, most which can be altered by alloying and production methods. Some of these properties include: low density, high corrosion resistance, reflectivity, conductivity, non-toxicity, high strength (only alloys) and formability. This has made aluminium one of the most used metals on the planet, second only to iron, and it is used everywhere from packaging to aeroplanes, and from decorative to structural purposes.

History

The existence of the metal aluminium was discovered by Sir Humphry Davy in 1808. However, it was not successfully separated into its pure form until 1825 by the Danish scientist Hans Christian Ørsted. The process he used was complicated and resource demanding, but in 1854 Henri Sainte-Calire found a much cheaper method for extraction, which allowed for the first commercial production of aluminium. This process was still costly and aluminium was an expensive metal primarily used for jewels and decorations. This changed in 1886 when the development of the electrolysis process would open up for mass production of aluminium. The cost of aluminium went from 28 000 \$/kg[1] in 1850 to 1 \$/kg in 1900 [1]. Since then the price has been relatively stable due to the combination of increasing demand and decreasing production cost.

The production of aluminium is closely linked to the availability of cheap electricity, due to the high energy cost of electrolysis. Norway has a access to a large

[1] prices in 2005 US dollar

amount of cheap hydroelectric power, and has become the largest producer of aluminium in Europe and is responsible for 4% of the worldwide production [2].

While the energy cost of primary aluminium production is high, the recycling process is less costly. The largest energy need in aluminium production is for breaking up the stable aluminium oxides, which is not a problem after the pure metal has been produced, and the energy cost of recycling aluminium is only 5% of the cost of producing it from its natural form. There are also no changes in the properties of aluminium after recycling, so it can be recycled endlessly. The advantages of recycling is the reason that over 70% of all aluminium produced from minerals is still in use today [3].

Alloys and Heat Treatment

While pure aluminium experience minimal corrosion and is much lighter than steel, it lacks the strength to compete for structural purposes. In the early 1900s it was discovered that when mixed with small amounts of other metals the aluminium would achieve a much greater hardness after being heat treated. Some decades later the cause for this increase was found with X-rays and electron microscopy. The added elements in the aluminium alloy will grow into particles known as precipitates during ageing. Some of these have the shape of needles that grow along the aluminium lattice planes, and they function similarly to steel rods in reinforced concrete. Due to their influence on the aluminium alloys properties a lot of research has been committed to studying the development of various precipitates and the factors that controls them.

The KK-Prosject

The KK-project[2] is an joint project between Hydro Aluminium, Steertec Raufoss AS, NTNU and SINTEF to increase understanding and control over the nucleation of precipitates in age-hardenable Al-Mg-Si alloys. The goal is to gain knowledge of which properties of aluminium are controlled by which factors and to learn how to produce aluminium with specific properties. The factors that are studied are the effect of altering temperature and the time of different parts of the heat treatment, additional alloying elements, deformations of the material and control over the grain structure.

Some specific goals are the development of an alloy for internal car components, where a high temperature stability is needed of the alloy, and how to accelerate nucleation of desired precipitates in order to decrease production time.

This project has tested how germanium in Al-Mg-Si-Cu alloys would effect the high temperature stability for Al-Mg-Si-Cu alloys for up to 100 hours of over-ageing at 250°C. It has been shown that adding germanium will increase the hardness [4], but it is an expensive element and it was desirable to know how little of it is needed for an effect.

[2]KimdanningsKontroll = Nucleation Control

This Thesis

Chapter 2 deals with some facts about aluminium alloys, heat treatments, and describes the precipitate sequence, some hardening mechanisms and the electron microscope. In Chapter 3the experimental procedure and the alloys used is presented. Chapter 5 describes and discusses the results from the hardness test and the TEM and STEM images. Highlights of the primary discoveries are presented in Chapter 5.

Appendix A discusses differences in hardness data in old and new experiments. In Appendix B the calibration of the magnification in the TEM is described. All the hardness values for the experiments can be found in Appendix C and the TEM images can be found in Appendix D.

Chapter 2

Theory

One of the great strengths of aluminium alloys is the great variety of properties they can posses by altering small parts of their composition and production. The main contribution to their strength comes from precipitates that develop after the solution heat treatment. Precipitates are microstructural particles with a different structure than the aluminium matrix. In this project the hardness during over-ageing is tested and the development of precipitates is studied using a transmission electron microscope (TEM). Some of the precipitates are studied using a scanning transmission electron microscope (STEM).

2.1 Aluminium Alloys

Aluminium alloys are generally divided into two main categories: wrought and cast alloys. Wrought alloys are formed by various types of mechanical deformation, e.g. extrusion and rolling. While cast alloys are too brittle to be shaped by deformation and are cast directly into their final form. Alloys are then classified by their composition. In the Aluminum Alloy Designation System four digits are used to identify the alloy [5]. For wrought alloys the first digit determines the main alloy element(s), the second defines variations of the initial alloy, while the last two digits are used to identify the specific alloy. In table 2.1 the main categories for wrought alloys can be seen with some of their main properties. There is a similar four digit system for cast alloys, but with a decimal point before the last digit.

2.1.1 6xxx Alloys

The alloys used in this project are of the 6xxx series (Al-Mg-Si alloys). This series has a combination of many good properties which make them ideal for a variety of purposes in marine, automotive, and building application. The specific type of alloys in the KK project are variations of the 6082 alloy. These alloys have added copper, a varying Si/Mg ratio and, for some, added germanium. Table 3.1 shows the composition of the alloys used in this thesis.

Table 2.1: ***Overview of the Aluminum Alloy Designation System and the properties of the different series [6, 7].***

	Major alloying elements	Properties
1xxx	Pure aluminium (> 99% Al)	Very low strength. High formability, corrosion resistance, and thermal- and electrical conductivity.
2xxx	Copper (and Magnesium)	High strength.
3xxx	Manganese	High formability and corrosion resistance.
4xxx	Silicon	Low ductility and formability. Good flow characteristic.
5xxx	Magnesium	Excellent corrosion resistance. Good formability, toughness and weldability.
6xxx	Magnesium and Silicon	High strength. Excellent extrudability. Good formability, corrosion resistance and weldability.
7xxx	Zinc and others	Very high strength.
8xxx	Other	Depends on alloying element
9xxx	Reserved for future use	

The 6xxx alloys are age-hardenable. This means that if they are heat treated they will experience an increased hardness due to the growth of precipitate that interact with dislocations in the matrix.

2.2 Heat Treatment

Another aspect which defines the properties of aluminium alloys is the way they are treated after they are cast or wrought. The properties of some of the alloys change greatly if subjected to treatment after they are fabricated. The type of treatment an alloy has been subjected to is defined by a temper designation, which consists of a letter, and sometimes a number to define the specifics of the treatment [5]. The letters are:

F, As fabricated

O, Annealed

H, Strain-hardened (only wrought alloys)

W, Solution heat treated

T, Solution heat treated and aged

2.2.1 The T6 Temper

The heat treatment used for the alloys in this project is the T6 temper. This means that the alloy has been subjected to solution heat treatment before it is artificially aged at a temperature above room temperature. Fig. 2.1 shows an overview of the procedure. In addition there is a room-temperature storage between the solution heat treatment and the artificial ageing. This is not a part of the T6 temper, but is a consequence of the fact that it is not practical for the industry to move tons of aluminium instantaneously between the two processes.

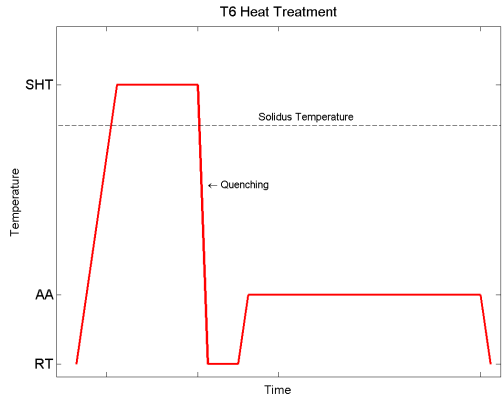

Figure 2.1: ***The T6 heat treatment. SHT: Solution heat treatment, RT: Room Temperature storage, AA: Artificial Ageing.***

The temperatures and lengths for the different treatment steps are dependent on the type of alloy and the desired properties of the final product.

Solution Heat Treatment

The solution heat treatment consists of heating the alloy to a temperature where the alloy elements are dispersed throughout the aluminium matrix. This means subjecting the alloy to a temperature where the aluminium is fully solidified while all the alloy elements are fully dissolved throughout the matrix, i.e. above the solidus line and below the liquidus line. This would be the T_0 shown in Fig. 2.2. The phase diagram shown is for a binary alloy at equilibrium, and is meant as a visual aid rather than an actual description of the phase diagram for aluminium alloys.

Quenching

If the alloy is slowly cooled to the T_2 in Fig. 2.2, the solute elements will start to nucleate in the matrix. There would then be both α (aluminium) and equilibrium β (alloy elements) phases in the matrix. The β phase will be large particles with a different structure than the aluminium lattice and its presence will weaken the

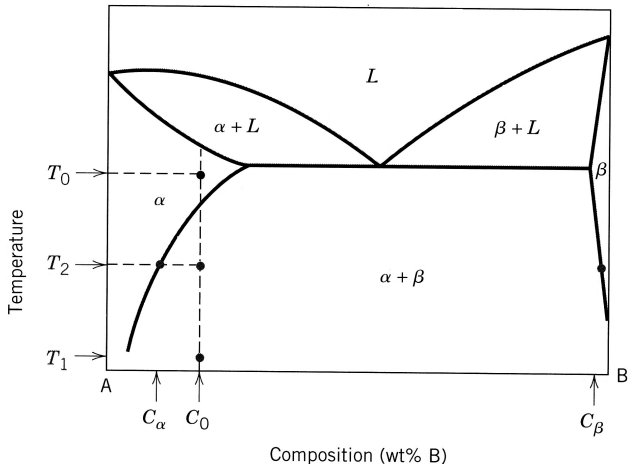

Figure 2.2: ***Hypothetical phase diagram for a binary alloy, with alloying composition C_0, at equilibrium. The α phase represents aluminium, while the β phase represents the equilibrium phase of the alloy element B. The actual phase diagrams for aluminium alloys with more elements are far more complex. [8].***

lattice. Instead the alloy should be quickly quenched to the T_1 in Fig. 2.2. This way the alloy elements have no time to nucleate and form β phases and instead they will be looked in the aluminium lattice, as seen in Fig. 2.3. Since the amount of solute elements in the aluminium lattice now are much greater than what it would be at the equilibrium level this is called a supersaturated solid solution (SSSS).

The equilibrium level for vacancies increases exponentially with temperature, and the sudden quenching will create a supersaturated level of them in the matrix. The vacancies are important for the early development of precipitates.

Room Temperature Storage

Room temperature storage is also known as natural ageing, as the alloy ages as it would in normal conditions. The SSSS has a higher energy level than equilibrium and the solute elements will start to cluster and nucleate in order to lower the total energy of the system. The diffusion process at room temperature is slow and a very long time will be needed before the system reaches equilibrium.

During room temperature storage the vacancies will disappear (e.g. by diffusion to grain boundaries). The vacancies will allow for substitutional diffusion of the solute elements and will increase the nucleation of some early precipitates. The amount of vacancies left when the artificial ageing starts will affect the later development of the alloy [9].

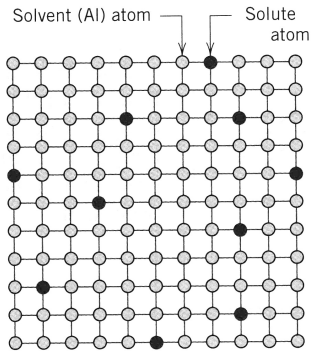

Figure 2.3: ***The super saturated solid solution. There will also be some vacancies (missing atoms) in the matrix in addition to the solute atoms. [8] .***

Artificial Ageing

The term *artificial* refers to the fact that the ageing process is artificially accelerated by heating the alloy. Different precipitates nucleate with greater intensity at different temperatures, so the temperature and length of the ageing will determine the final properties of the alloy. The artificial ageing is normally continued until the alloy reaches its peak hardness.

Over-Ageing

When the alloy is artificially aged after it has reached its peak hardness it is called over-aged and will lose it hardness and strength. If it is over-aged long enough, the nucleation will reach equilibrium and the properties of the alloy will stop changing.

2.3 Crystal structure

Aluminium has a face-centered-cubic (FCC) crystal structure. This means that the smallest repeating structure in the aluminium lattice is a cube with one atom in each corner and one on each side of the cube as shown in figure 2.4.

The orientation of the lattice is important when studying the atomic structure of a material, since a structure can look completely different from a different angle. The lattice vectors are used for defining positions in a crystal. For a cubic crystal this is simple as the lattice vectors go along the edges of the cubic unit cell as they would in a Cartesian coordinate system.

A plane in the lattice is defined by the three points were the plane intercept the lattice vectors. These points are the lattice constants a_1, a_2 and a_3, which are multiples of the lattice unit vectors $\mathbf{a}_1$, $\mathbf{a}_2$ and $\mathbf{a}_3$. It is common to use the Miller indices (hkl) to denote the plane. These are found by taking the smallest ratio of the reciprocal of the lattice constant. An example is shown in Fig. 2.5. If a plane do not intercept one of the lattice vectors then the related Miller index is 0, and a

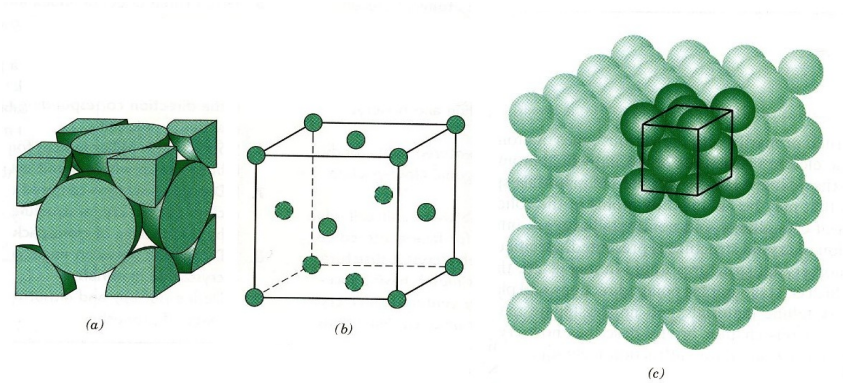

Figure 2.4: ***The face-centered-cubic crystal structure. (a) hard-sphere unit cell representation, (b) reduced-sphere unit cell, (c) a FCC crystal. [8].***

negative value is denoted by an overbar ($-1 = \overline{1}$). Some examples of lattice planes can be seen in Fig. 2.6.

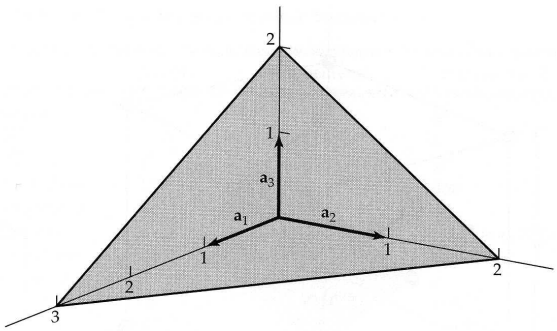

Figure 2.5: ***A plane which intercepts the lattice vectors at*** $3\mathbf{a}_1$, $2\mathbf{a}_2$ ***and*** $2\mathbf{a}_3$***. This gives the reciprocal numbers*** $\frac{1}{3}$, $\frac{1}{2}$, $\frac{1}{2}$, ***and the numbers that have the smallest common ratio are*** $2, 3, 3$, ***which means that this is a*** (233) ***plane. [10].***

A direction in the lattice is denoted by $[uvw]$ where u, v, w are the smallest integers which defines a vector $\mathbf{r} = u\mathbf{a} + v\mathbf{b} + w\mathbf{c}$, along the direction. For cubic crystals the $[hkl]$ direction will be perpendicular to the (hkl) plane. Due to the symmetry of the aluminium lattice there are no differences between the [100], [010] and [001] directions, and this set of direction is denoted as $\langle 100 \rangle$.

In this work all the specimens were studied along the $\langle 100 \rangle_{\mathrm{Al}}$ zone axis.

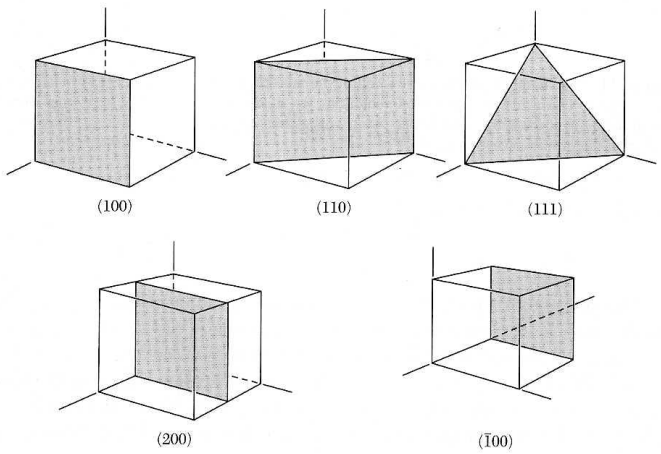

Figure 2.6: ***Various lattice planes for cubic crystals. [10].***

2.4 Hardening Mechanisms

Hardness is defined as a material's resistance to localized plastic deformation. Plastic deformation is when a material subjected to an external force will not recover its original shape after release, e.g. dents or scratches. When a crystalline material is subjected to a plastic deformation, there will be a slip in the matrix as one part of the crystal matrix moves while the rest is in place. In order for a slip to occur the energy required to shift the matrix must be less than the energy submitted by the force working on the material.

The aluminium matrix is not a perfect crystal and contains dislocations. These are "errors" in the lattice, where the lattice plane is discontinuous between two parts of the matrix. This can either be a missing atom in the matrix, too many atoms in the matrix, a bend of the matrix or a lattice plane that ends within the matrix. The first two are called point defects, while the latter two are respectively called a screw dislocation and an edge dislocation. Fig. 2.7 shows the slipping of an edge dislocation. Dislocations have a strain field caused by the discontinuous lattice plane. When this strain field interacts with other strain fields in the matrix there will be a resistance. The energy needed for deformation will increase and the material will be harder. There are many ways strain fields can occur in materials and some will be presented here.

The strength of the FCC crystal lattice is low, and pure aluminium is a soft metal. By adding solute elements to the aluminium matrix and heat treating the alloy it is possible to increase the hardness due to the interaction of the strain fields from the precipitates and dislocations.

In figure 2.8 the general stages of hardness mechanisms in a solution heat treated aluminium alloy can be seen. The four different mechanisms are solute hardening, coherency strain, chemical hardening and dispersion hardening. They take place on different times as they are caused by different types of precipitates which exist

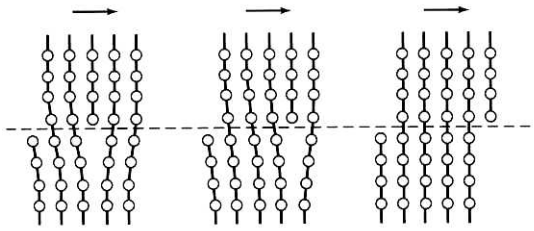

Figure 2.7: ***Movement of an edge dislocation due to external stress on the matrix. [10]***

at different stages. Altering parts of the heat treatment changes which precipitates grow more favourably and will change how much each hardening mechanisms will influence the total hardness.

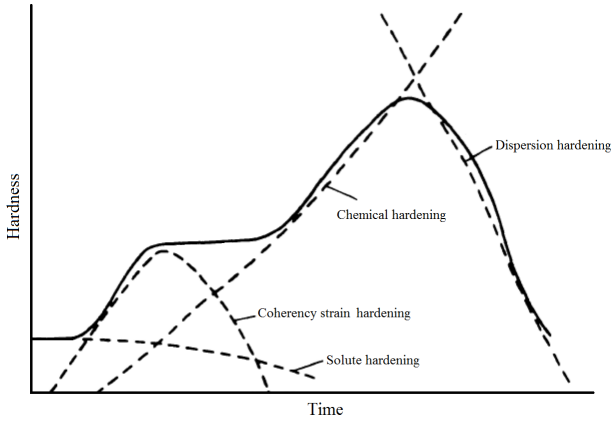

Figure 2.8: ***Hardness curve during precipitate hardening. Shape can differ for different aluminium alloys. Based on picture from [6].***

2.4.1 Solute Hardening

After the solution heat treatment the alloying elements will be spread substitutionally throughout the matrix replacing aluminium atoms, as shown in Fig. 2.3. These solute elements are generally not the same size as the aluminium atoms, so there will be a lattice strain caused by too small or too big atoms in the lattice, Fig. 2.9.

Over time this effect will become less dominant, as the alloy elements will start to cluster and nucleate into precipitates.

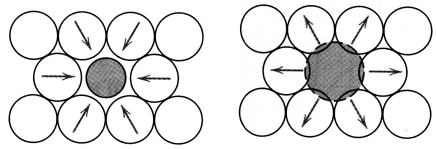

(a) (b)

Figure 2.9: ***Strain stress from solute atoms in an alloy. [8].***

2.4.2 Coherency Strain

The next dominant hardening effect is caused by the development of the coherent precipitates. Coherency is a difference in the crystal structure of two phases at their interface. The less coherent a precipitate is, the less continuous the lattice planes are over the interface. A fully coherent precipitate will have the same crystal structure as the surrounding matrix while an incoherent precipitate will have a completely different structure, Fig. 2.10.

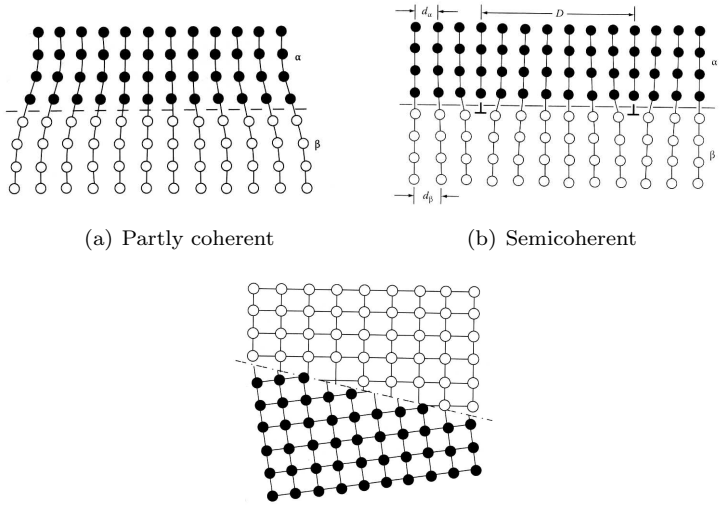

(a) Partly coherent (b) Semicoherent

(c) Incoherent

Figure 2.10: ***Different levels of coherency of an α and β phase. [11]***

Partly coherent precipitates will be surrounded by a strain field caused by a difference in the matrix of the precipitate and the rest of the material. Semicoherent and incoherent precipitates have a smaller strain field since it is not possible to match the lattice planes of the matrix and the precipitate, and so there is less strain from bent lattice planes.

The hardness from the coherency strain is not linear to the number of coherent precipitates. In Fig. 2.8 the shape of the coherency strain effect can be seen to be parabolic. At the start of the curve there are numerous small and partly coherent precipitates. The combined effect of all the strain field will create both a pushing and pulling effect on the dislocations. The two forces will cancel each other out and the result will be a weak hardening effect. At the top of parabolic hardness curve the precipitates have become larger and more dispersed and the distance between the strain fields is large enough for the dislocations to only be affected by the fields holding them back [6]. Fig. 2.11 shows a approximate picture of this. When the precipitate density is even lower the dislocations will be able to bend around the strain fields and the coherency strain will stop contributing to the total hardness.

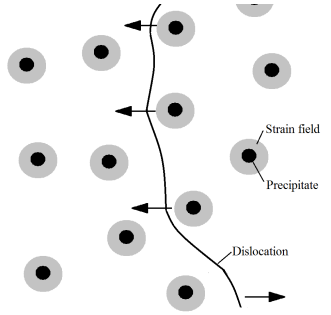

Figure 2.11: ***Example of how a dislocation can be hold back by the strain fields from coherent precipitates.***

2.4.3 Chemical Hardening (Cutting)

It is possible for dislocations to cut through the precipitates. This will, as shown in Fig.2.12, offset the precipitate. The energy required to achieve this is dependent on the size and form of the precipitate and the interfacial energy of the new area formed between the precipitate and the matrix [12].

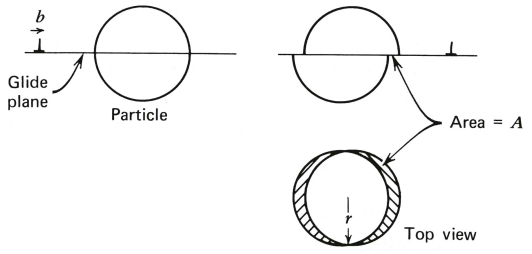

Figure 2.12: ***The cutting of a precipitate by a dislocation*** b***, [12].***

As the precipitates become larger and less coherent, the energy required to cut

through the precipitate eventually becomes too large for cutting to be energetically favourable.

2.4.4 Dispersion Hardening

As the precipitates grow they will become too large to be cut by the dislocations and the dislocations will instead bow around the precipitates. This can either cause the dislocation to change shape as it bends to get past the precipitate, or it can loop around the precipitate as seen in Fig. 2.13. The looping can occur several times with subsequent dislocations going around the previous ones, increasing the density of dislocations. This hardness effect is greatest for spread precipitates and becomes less effective as the precipitates continue to grow, as the amount of bending the dislocation must do to get around the precipitates increases [12].

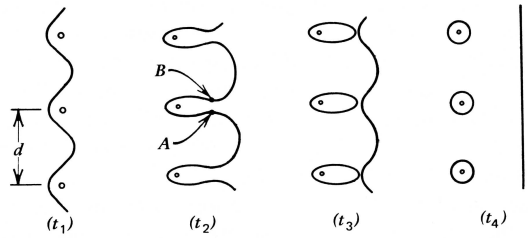

Figure 2.13: ***Interaction between a dislocation and a row of precipitates, [12].***

As Fig. 2.8 shows, the hardening effect from the precipitates will eventually disappear as the precipitates become too large and the precipitates only coarsen the matrix and reduce its strength.

2.5 Precipitate Development

The general precipitation sequence for aluminium alloys after the solution heat treatment is:

SSSS → Atomic clusters → Metastable Phases → Stable Equilibrium Phase

After the solution heat treatment and the quenching, all the alloying elements will be spread through the matrix as in Fig. 2.3. Since this structure is above the equilibrium level, the solute elements will start to nucleate into small clusters. The composition of these clusters will depend on the alloy composition and their solubility.

A large amount of aluminium research is targeting the metastable intermediate phases due to their importance in determining the properties of the aluminium alloy. The precipitates consist of various combinations of the elements in the alloy. Some precipitates contain aluminium, while some only consist of the different alloy elements.

The density and size of different precipitates are dependent on the temperature of the artificial ageing and the length of the natural and artificial ageing. This is due to the different activation energies required for the formation of precipitates and the density of previously formed precipitates.

Al-Mg-Si alloys

The following precipitate sequence has been found for 6xxx alloys [13]:

$$\text{SSSS} \rightarrow \text{Atomic clusters} \rightarrow \text{GP zones} \rightarrow \beta'' \rightarrow \beta',\ \text{U},\ \text{B}' \rightarrow \beta,\ \text{Si (stable)}$$

For 6xxx alloys there will initially be a nucleation of Si clusters which later form Mg/Si clusters [14]. From these clusters the GP zones[1] will form. The GP zones are small (1–3 nm) partly coherent precipitates. They will function as nucleation sites for β'' precipitates. β'' precipitates are sometimes referred to as GP-II zones as they are both coherent and small precipitates. In 6xxx alloys it has been found that the GP zones and β'' precipitates are the main hardening phases [15].

As over-ageing continues, new precipitates develop and the effect of the coherency hardening decreases as more semi- and incoherent precipitates develop. Eventually stable precipitates like the β and Si phases will develop and a equilibrium will be reached. These are large plate-like precipitates that reduce the strength of the alloy.

A list over the precipitates in Al-Mg-Si alloys can be seen in table 2.2.

Table 2.2: ***Phases observed in aged Al-Mg-Si alloys. Size of precipitates is only a rough approximation. [13, 14, 16, 17].***

Phase	Composition	Morphology	Structure
GP	$Mg_xAl_{5-x}Si_6$	Ranging from spheres of a few nm to needles of $\sim 2x2x20$ nm	Monoclinic, $C2/m$
β''	Mg_5Si_6	Needles of $\sim 4x4x50$ nm	Monoclinic, $C2/m$
β'	$Mg_{1.8}Si$	Rods hundreds of nm long and diameters of ~ 15 nm to ribbons several μm long	$P6_3$
U1	$MgAl_2Si_2$	Needles hundreds of nm long and diameters of ~ 15 nm	Trigonal, $P_{\bar{3}m1}$
U2	MgAlSi	Needles hundreds of nm long and diameters of ~ 15 nm	Orthorhombic, P_{nma}
B′	$Mg_9Al_3Si_7$	Ribbons up to $\sim 1\mu$m	Hexagonal
β	Mg_2Si	Plates or cubes of 10–20 nm	$F_{m\bar{3}m}$
Si	Si	Plates	F_{d3m}

[1] Named after Guinier and Preston who both discovered their existence independently

Al-Mg-Si-Cu alloys

When copper is added to Al-Mg-Si alloys there will be different precipitates present, and the following precipitation sequence has been observed [16]:

$$\text{SSSS} \rightarrow \text{Atomic clusters} \rightarrow \text{GP zones} \rightarrow \beta'',\ \text{L},\ \text{QP},\ \text{QC},\ \text{C} \rightarrow \beta',\ \text{Q}' \rightarrow \text{Q}$$

There is less data on the Al-Mg-Si-Cu precipitation sequence than for the Al-Mg-Si, and not everything about the development is known. A list describing them can be seen in table 2.3. It is believed that the QP, QC and L phases are the predecessors of the Q′ phase, which eventually becomes the stable equilibrium phase Q [16, 18]. The L phase has no ordered structure, while the rest have a hexagonal sub-lattice ($a_1 = a_2 = 3.93$ Å, $a_3 = 4.05$ Å)[16]. The C precipitate is plate shaped, while the rest has a needle-like morphology growing along the $\langle 100 \rangle_{\text{Al}}$ direction.

Table 2.3: ***Phases observed in aged Al-Mg-Si-Cu alloys, [16, 19].***

Phase	Composition	Morphology	Structure
L	Unknown	Needle	Unknown
QP	Unknown	Needle	Hexagonal
QC	Unknown	Needle	Hexagonal
C	Unknown	Plate	Monoclinic
S	Unknown	Needle	Unknown (hexagonal)
Q′	Probably $Al_3Cu_2Mg_9Si_7$	Needle	Hexagonal, ($P\overline{6}$)
Q	Probably $Al_3Cu_2Mg_9Si_7$	Needle	Hexagonal, ($P\overline{6}$)

It is not believed that the β'' and GP zones are the main strengthening phases in the Al-Mg-Si-Cu alloys, since they are not the most abundant phases at the peak hardness. Instead it is most likely the Q′ predecessor L that is the main strengthening phase in Al-Mg-Si-Cu alloys [16, 18]. In this report it will primarily be the L and the Q′ precipitates that are studied. The L precipitates cross-section is elongated along the $\langle 100 \rangle_{\text{Al}}$, while the Q′ is mainly angled 11° to $\langle 100 \rangle_{\text{Al}}$, i.e. the $\langle 510 \rangle_{\text{Al}}$ direction [18].

Ge in 6xxx alloys

When germanium is added to Al-Mg-Si alloys, no large difference in the precipitation sequence has been observed, however, there will be some changes in the density and size of the precipitates. Silicon and germanium have similar properties, as they both are in the same column in the periodic table, and it has been shown that germanium will replace the silicon in the precipitates of Al-Mg-Si alloys [20].

Adding germanium to Al-Mg-Si-Cu has been shown to increase the hardness of the alloy [4], and the purpose of this thesis was to study how the effect of a low Ge-content (0.002–0.037 at.%). However, as noted in Chapter 4.4 and Appendix A, the assumed effect of the Ge-content may have been overestimated.

2.6 The Transmission Electron Microscop (TEM)

The human eye is capable of resolving objects down to 0.1–0.2 mm. In order to study smaller structures, a microscope is needed. The visible light microscope (VLM) is the most commonly known type of microscope. It magnifies an image of a sample, using optical lenses that bend the light reflected from the sample.

The limitation of a microscope is in the wavelength. If an object is smaller than half of the wavelength then the wave will not be reflected and it will not be possible to resolve the object. This means that a VLM will have a maximum resolution of 300 nm. In electron microscopes a focused beam of electrons is used instead of light, and magnetic fields are used as lenses. Theoretically it is possible to have an electron microscope with a resolution below 0.001 nm. This range has not been reached and electron microscopes today have normally "only" a resolution of 0.2 nm (0.05 nm at best). This resolution still makes the TEM an excellent tool for studying the atomic structures of material and it is commonly used in medical, biological and materials research. While the first electron microscope was built in 1932 they are still a new invention compared to the 350 years of development behind the VLM, and they are continuously being improved.

The transmission electron microscope (TEM) functions by letting the electrons pass through the specimen. The interactions between the electrons and the material create differences in the contrast, which results in an image that can be studied. A simple overview of a TEM can be seen in Fig. 2.14.

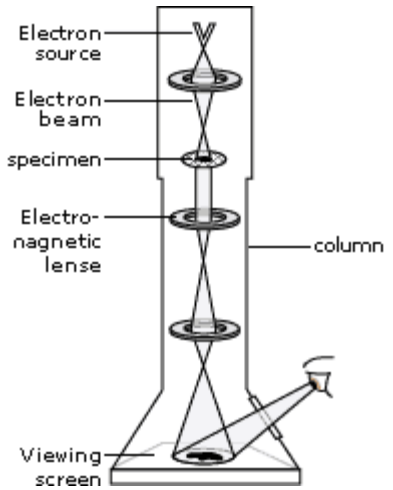

Figure 2.14: ***Schematic overview of a TEM. [21].***

The main parts of the TEM system are the electron gun, the magnetic lenses, the specimen holder and a detector/display. All of these parts are all enclosed by the column. **The electron gun** is used to create the electron beam. The electrons are emitted by either thermionic or field electron emission by subjecting the gun to a high voltage (100–300 kV). **The magnetic lenses** bend the electrons just as glass bends light. The advantage of the magnetic lenses is that they are fields which strengths can easily be adjusted. In Fig. 2.15 it can be seen how the electron beam is bent. In normal TEM mode a parallel beam of electrons is used. There are three different levels of lenses in the TEM, the condenser lenses, objective lenses and the projector lenses. The condenser lenses (C1 and C2 in Fig. 2.15) are used to focus the electron beam onto the specimen, the objective lenses are used to create a magnified image of the specimen, while the projector lenses are used to further magnify the image and project it to a detector/display. There are many different types of **specimen holders** that can be used in a TEM. Most are designed for a disc 3.05 mm in diameter, but there are exceptions. Holders are generally designed to allow for tilting of the specimen, and there are some that subject the specimen to various forces (e.g. twisting, compressing, heating, cooling). Since it is not possible for the human eye to see electrons, **a detector or a display** is needed to convert the electrons into something that can be observed. One way is to include a fluorescent screen in which the electrons excite the atoms and produce visible light. Another way is to use a detector which registers the electrons, both films and digital cameras are used for this. **The column** is the vertical structure that contains all the parts of the TEM. In order to prevent energy loss and scattering of the electrons, the column contains a vacuum. Since electrons are a form of ionizing radiation, enclosing the TEM also protects the user from radiation.

Electrons will generate some secondary signals when they interact with a material and they can also interact with themselves. This allows for the TEM to be more than just a microscope, and it can produce a large amount of information from the material.

2.6.1 Bright- and Dark-Field Imaging

By adjusting the objective aperture in Fig. 2.15 it is possible to select different parts of the electron beam. If all but the direct beam is blocked by the aperture it will mainly be the unscattered electrons that will make up the image. In this case the contrast in the displayed image will come from mass-thickness and diffraction contrast, and thicker areas and crystalline structures will appear dark. Since the image will be brightest with no specimen this mode is called Bright Field (BF). All the TEM images in the thesis were taken in BF mode.

Dark-Field (DF) is when the direct beam is blocked and only one of the diffracted beams pass through the objective aperture. In this mode most of the electrons have been scattered and the image will contain more information related to the structure of the specimen, as the electrons have experienced a greater amount of interaction with the material. Areas without structures to scatter the electrons will appear dark in the displayed image.

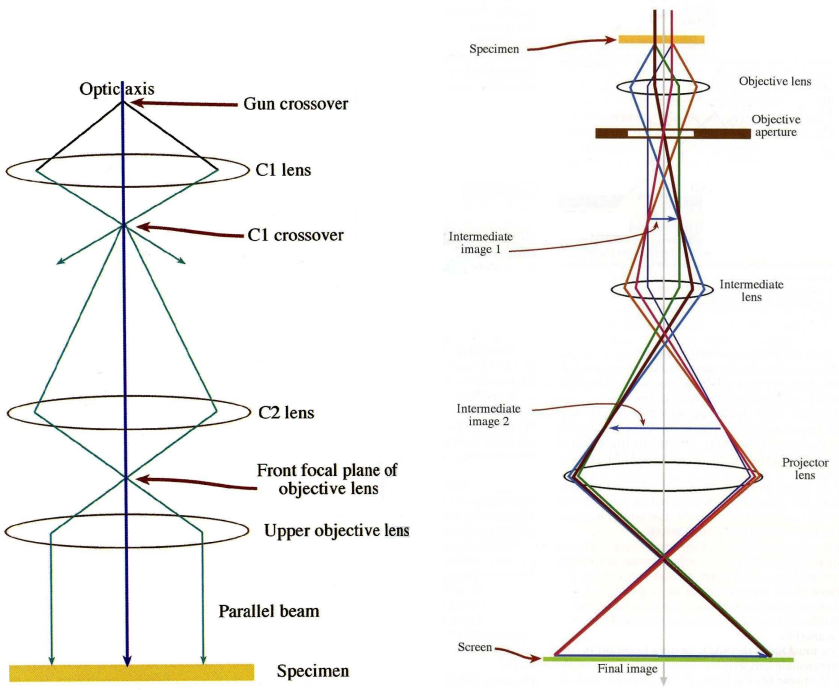

(a) Illumination system (b) Imaging system

Figure 2.15: ***The lens system in a TEM. The width of the electron beam is greatly exaggerated. [22]***

2.6.2 Diffraction

Diffraction is a result of the fact that electrons can interfere with each other. When the electron beam passes through a crystal structure, the electrons will be spread by a distance relative to the structure of the crystal. The electrons will then constructively or destructively interfere and a pattern will form. This pattern will be related to the specific crystal and can be used to identify the crystal structure of a specimen and its orientation.

In this thesis diffraction was used to find the $\langle 100 \rangle_{\mathrm{Al}}$ zone axis. The diffraction pattern of a FCC crystal along the $\langle 100 \rangle_{\mathrm{Al}}$ axis can be seen in Fig. 2.16.

2.6.3 (P)EELS

Parallel electron energy-loss spectroscopy is a technique that analyses how much energy the electrons lose as they pass through a specimen. As the electron interacts with the atoms in the specimen, they can lose energy through various forms of inelastic scattering. By determining how the electrons lose energy it is possible to get data on the material's chemical and physical structure.

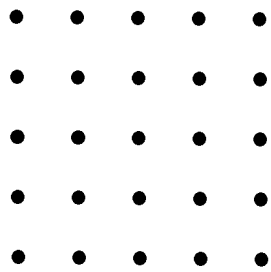

Figure 2.16: ***The diffraction pattern on a FCC crystal seen along the*** $\langle 100 \rangle_{Al}$ ***zone axis.***

The only feature used in this project is its ability to calculate a specimens thickness by measuring the amount of inelastic scattered electrons, which increases with the thickness.

2.6.4 EDX

Energy-dispersive X-ray spectroscopy analyses the X-rays that are generated when electrons are inelastically scattered in a material. Since the X-rays generated have a spectrum related to the atomic elements, it is possible to determine the elements present in the area hit by the electron beam.

2.7 STEM

In scanning transmission electron microscopes (STEM) a thin beam of electrons is scanned over an area of the specimen. The beam is convergent, as opposed to the parallel beam in TEM, and Fig. 2.17 shows how the convergent beam is created. As the beam interacts with atomic columns with different compositions the beam will be scattered differently and this will create the contrast in the final image. Different detectors will continuously detect the scattered electrons as seen in Fig. 2.18. In STEM the resolution is not limited by the magnetic lenses, but by the size of the electron beam. Each scanned point on the specimen generates a signal that is detected and amplified before displayed at a corresponding position on the displayed image. The image builds up as the scanning continues.

In this thesis High-Angle Annular Dark-Field STEM (HAADF-STEM) was used. *Dark-Field* means that all unscattered electrons are excluded, the word *Annular* refers to the fact that the detector is a disc around the direct beam, as seen in Fig 2.18, and *High-Angle* means that only highly scattered electrons are detected. With this technique Rutherford scattering [2] will allow for Z-contrast[3] in the image. This is very useful for Al-Mg-Si-Cu alloys, since copper has a much higher atomic number than the rest of the elements present, and will be much

[2]Incoherent elastic scattering due to interaction with the Coulomb forces of the nuclei
[3]Z is the atomic number of an element

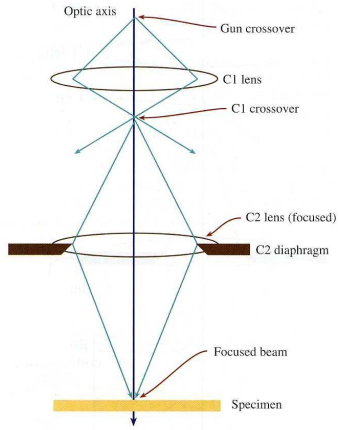

Figure 2.17: ***Convergent beam mode in a TEM. The non-parallel convergent beam is used for the scanning in STEM. [22].***

brighter in the final image. $Z_{Cu} = 29$ compared to $Z_{Mg} = 12$, $Z_{Al} = 13$ and $Z_{Si} = 14$. Germanium should also be observable, with $Z_{Ge} = 32$, but will be hard to distinguish from the copper.

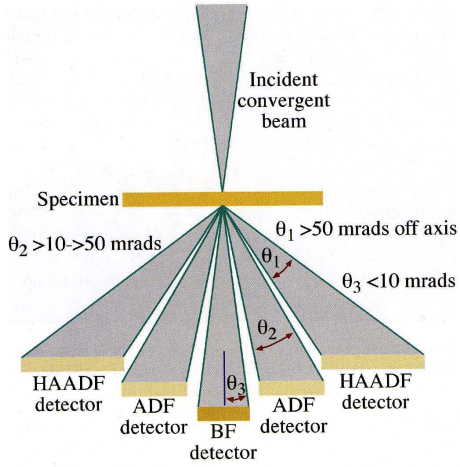

Figure 2.18: ***Different detectors in a STEM. BF = Bright-Field, ADF = Angular Dark-Field, HAADF = High-Angle Angular Dark-Field. [22].***

Chapter 3

Experiment

3.1 Experimental Procedure

The alloys came as long rods of extruded aluminium with a diameter of 20 mm, Fig. 3.1(a), and were treated as follows:

1. 120 mm long cylinders were cut from the rods
2. Heat treatment (T6)
   (I) Solution heat treatment (530°C salt-bath for 30 min)
   (II) Water quench (Room temperature)
   (III) Natural ageing (Room temperature for 4 hours)
   (IV) Artificial ageing (155°C oil-bath for 12 hours)
   (V) Water quench (Room temperature)
3. 10 mm long samples were cut from the 120 mm long cylinders
4. Over-ageing
   (I) Grinding and hardness testing
   (II) Over-ageing (250°C sand-bath)
   (III) Water quench (Room temperature)
   (IV) Repeated for increasing over-ageing time-steps

The hardness was tested after 15min, 30min, 1h, 1.5h, 2h, 3h, 4h, 5h, 7h, 10h, 15h, 24h, 48h, 72h & 100h of over-ageing. The same samples were used for the entire over-ageing series.

The remaining part of the heat treated 120 mm cylinders were kept in case some part of the over-ageing would be needed to be done again.

Two stages of the over-ageing were chosen to be studied in the TEM: 24 hours and

(a) Original rods (b) 120 mm rods

Figure 3.1: ***The four aluminium rods before heat treatment.***

100 hours of over-ageing. The 24h samples were taken from the same samples used in the hardness testing, while the 100h samples were over-aged the full 100 hours in one time-step. The TEM specimens were prepared as follows:

1. A thin disk of 20 mm diameter were cut from the sample
2. The disc was ground and polished down to an approximate thickness of 100 μm
3. 3 mm specimens were punched from the disk
4. Electropolishing of specimens

3.2 Alloys

The composition of the alloys studied in this thesis can be seen in table 3.1. The KK3x series is used to study the effect of germanium in Al-Mg-Si-Cu alloys. They possess a varying amount of germanium which replaces the silicon. The series is based on the KK1 alloy which has no germanium.

In addition to the four KK3x alloys, two KK13 and KK24 cylinders and a 10 mm long KK1 sample was included in the heat treatment. The reason for this was to get new hardness data, as it appeared that the old data at 250°C was erroneous. This is discussed in Appendix A. KK13 alloy has a greater Mg/Si ratio than the KK1, and the KK24 is the KK13 with Ge replacing some Si.

3.3 Heat Treatment (T6)

In Fig. 3.2 an overview of the T6 heat treatment is shown. This treatment is meant to make the alloys reach the peak hardness condition (T6) before the start of the

Table 3.1: ***Alloy compositions in weight and atomic percentage.***

Alloy	Si	Mg	Cu	Fe	Mn	Ge
KK1 wt%	0.64	0.90	0.40	0.20	0.55	-
KK1 at%	0.62	1.00	0.17	0.10	0.27	-
KK13 wt%	0.52	1.01	0.40	0.20	0.55	-
KK13 at%	0.50	1.13	0.17	0.10	0.27	-
KK24 wt%	0.47	1.01	0.40	0.21	0.55	0.13
KK24 at%	0.45	1.13	0.17	0.10	0.27	0.05
KK30 wt%	0.603	0.896	0.398	0.206	0.547	0.100
KK30 at%	0.583	1.000	0.170	0.100	0.270	0.037
KK31 wt%	0.622	0.896	0.398	0.206	0.547	0.051
KK31 at%	0.601	1.000	0.170	0.100	0.270	0.019
KK32 wt%	0.635	0.896	0.398	0.206	0.547	0.019
KK32 at%	0.613	1.000	0.170	0.100	0.270	0.007
KK33 wt%	0.640	0.896	0.398	0.206	0.547	0.005
KK33 at%	0.618	1.000	0.170	0.100	0.270	0.002

over-ageing.

Salt-Bath

A picture of the salt-bath used is shown in Fig. 3.6(b). While the temperature of the bath was stable, the cylinders were large enough for the bath to cool down when they were inserted. The temperature would initially drop to around 500°C, then after 10 minutes it would be close to 520°C, and within 30 minutes, the temperature would be at 530 ± 5°C.

Room Temperature

The samples were left in the same room as the salt- and oil-bath, where there was a stable temperature at 23 ± 1°C.

Oil-Bath

The oil-bath contains Wacker AP 200 Silicone Fluid, and a picture of it is shown in Fig. 3.6(c). The oil-bath reached the correct temperature of 155 ± 1°C in little over five minutes after the insertion of the cylinders.

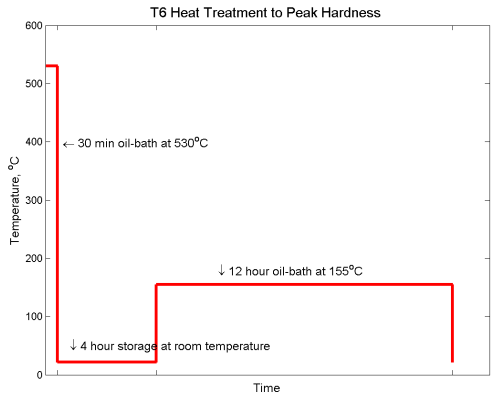

Figure 3.2: ***The T6 heat treatment used. After each of the baths the samples were water quenched.***

3.4 Hardness Testing

There are several different scales of hardness testing. Early tests for hardness were based on a material's ability to scratch another material [8]. One of these tests is the Mohs scale, which goes from 10 (diamond) to 1 (talc). More quantitative scales have later been developed. They mainly make use of an indenter to make a small dent in the sample, and the size of the dent is then used to determine the hardness. The shape and the material of the indenter and the load weight vary for different types of testing methods. Hardness values are generally denoted by the type of test and the load used.

For aluminium alloys the Vicker hardness test (HV) is a good choice. It uses a pyramid shaped diamond indenter with a slope of 136° pressed down with a load F, seen in Fig. 3.3. From the load and the surface area of the indentation, the hardness is calculated:

$$\mathrm{HV}F = \frac{\text{Load}}{\text{Surface area}} = F \cdot \frac{2 \cdot \sin(136°/2)}{d^2} = 1.8544 \frac{F}{d_1 \cdot d_2},$$

where d_1 and d_2 are the diameters of the indentations.

To reduce the error, 10 indentations were made on each sample, 5 on each flat side of the cylinder. The indentations were made in the area of 2 mm from the center and 3 mm from the edges of the sample. The distance between two indentations was generally longer than 3 mm. An example of a sample with indentations can be seen in Fig. 3.4.

The machine used to measure the hardness was a Duramin A2500, Fig. 3.5.

Due to the large shift in hardness during the over-ageing, it was necessary to change from HV5 to HV1 after 24 hours of over-ageing. For most metals there

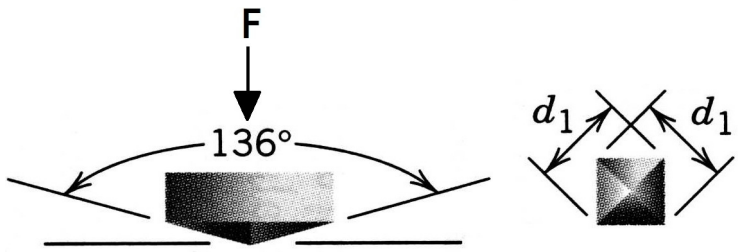

Figure 3.3: ***Vicker hardness testing technique. F is the weight of the load on the indenter and d_1 and d_2 are the diameters of the indentations. [8].***

Figure 3.4: ***Picture of one sample with indentations made by the hardness tester.***

should not be a too large difference between measurements done at HV1 and HV5. The hardness was tested with both HV1 and HV5 at the 24 hour mark, and table C.1 and C.2 show a lower hardness with HV1 for most of the alloys. However, as all the alloys compared were tested in the same manner, it would not affect the comparing of the results.

Error Calculation

The mean of the 10 indentations is used as the hardness for each over-ageing step. The standard error of the mean (SEM) is used to calculate the error with the formula:

$$SEM = \frac{s}{\sqrt{n}}, \tag{3.1}$$

where n is the number of measurements and s is the sample standard deviation:

$$s = \sqrt{\frac{1}{(n-1)} \sum_{i=1}^{n} (\bar{x} - x_i)^2}. \tag{3.2}$$

x_i is the measured values and $\bar{x} = 1/n \cdot \sum_{i=1}^{n} x_i$ is the mean.

Figure 3.5: ***Duramin A2500 hardness tester***

3.5 Grinding

As the same sample was used for each time-step, it was necessary to grind down the surface of the samples to make room for new indentations. This was done after the over-ageing step and before the hardness was tested.

The final grinding step during the HV5 hardness tests was done with P1200 silicone carbine grinding paper, with an average particle diameter of $\sim$15 μm. This paper was chosen because it gave clear and visible indentations during the hardness testing. When the load changed after the 24 hour mark, it became necessary to use P4000 grinding paper ($\sim$2.5 μm particle diameter) since the indentations were smaller. As the hardness decreased and the indentations became larger, the P4000 grinding paper continued to be used. No clear change of the error in the measurements was observed.

3.6 Sand-Bath

The sand-bath used in the over-ageing can be seen in Fig. 3.6(a). The bath has heating elements and a constant flow of air through the sand. If the airflow was not properly adjusted, it was noted that the temperature gradient could be large. When the flow was correct the temperature was stable at 250 ± 2°C. Fig. 3.7 shows some of the temperature measurements made during the over-ageing. More measurements were made at later stages of over-ageing, but showed no deviation greater than ± 2°C.

(a) Sand-bath

(b) Salt-bath

(c) Oil-bath

Figure 3.6: ***Pictures of the various baths used for the heat treatments of the samples.***

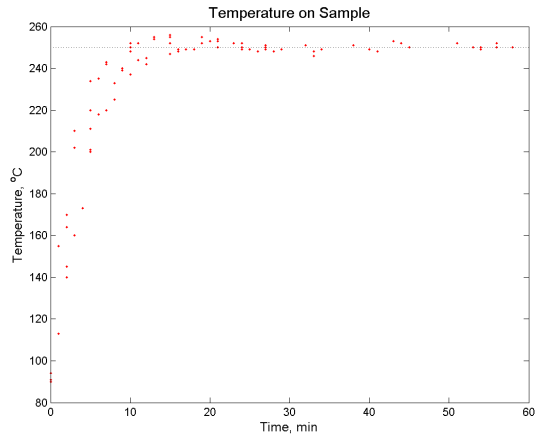

Figure 3.7: ***The temperature measured on samples after insertion for various over-ageing steps in the sand-bath. Dotted line is the 250°C mark.***

3.7 Specimen Preparation

In order to study materials in a TEM the specimens must be electron-transparent, which means that the aluminium specimens must be less than 100 nm thick. This thickness cannot be reached just by cutting the sample. How to get a sample electron transparent depends greatly on the type of material studied and what one wishes to study. Generally the process starts with creating a very thin specimen that fits into the holder used in the TEM, normally 3.05 mm in diameter. This can be done by cutting a specimen from a bulk sample or shaping ground material. While the pre-thinning can be done by mechanical means, the final thinning from micrometers to nanometres must be more delicate. It can be done with ion-milling or with electropolishing.

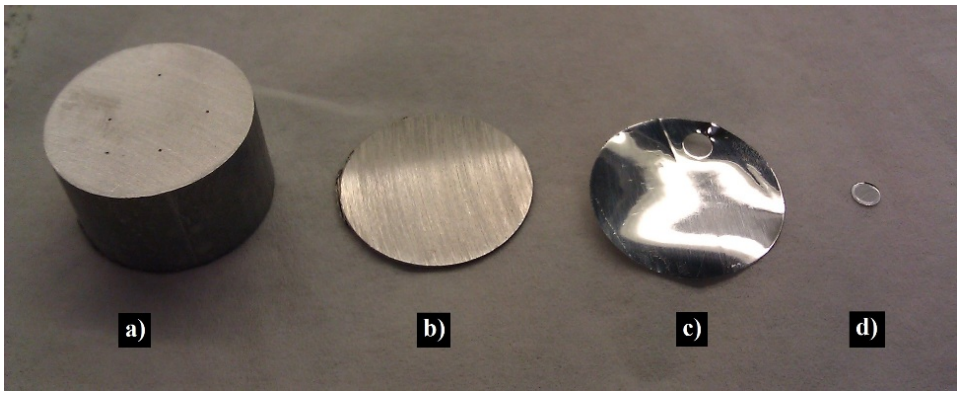

Figure 3.8: ***The various stages of specimen preparation. a) Sample. b) Cut disk. c) Thinned disk. d) TEM specimen.***

3.7.1 Cutting

The samples were first cut into thin disks of a few hundred micrometers, Fig. 3.8(b). They were then ground down to around 100 μm and polished with P4000 silicone carbine grinding paper, Fig. 3.8(c).

3.7.2 Stamping

3 mm in diameter specimens were stamped out from the thin disk using a Gatan Disk Punch, Fig. 3.9. Each disk gave 15–20 specimens, Fig. 3.8(d).

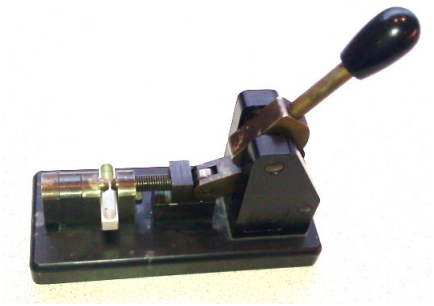

Figure 3.9: ***The mechanical punch used to cut the 3 mm specimens.***

3.7.3 Electropolishing

Electropolishing is a simple way to do the final thinning if the samples are electrically conducting. The process works by applying a voltage to the specimen while it is in an electrolyte solution. If the ratio of the voltage and current between the specimen and electrolyte is correct, the anodic dissolution of the specimen can polish the sample very accurately.

A twin-jet electropolisher unit, Fig. 3.10, pumps two jets of electrolyte at the specimen from both sides, with the specimen suspended in a Teflon holder in the middle. A sensor measures the transparency of the specimen. If the electropolishing has been successful there will then be a hole in the sample as seen in Fig. 3.11. At the edge of this hole the thickness of the specimen will be what is needed for good results with the TEM. This area at the edge is small and less than 10 μm from the edge the specimen will generally be too thick for any good pictures.

A TenuPol-5 electroplishing unit was used with a mix of 1/3 nitric acid and 2/3 metanol as the electrolyte, and a temperature of -25°C to -20°C was maintained using liquid nitrogen.

There are several conditions that need to be in place for the best results, most of which are difficult to control. The initial thickness of the specimen, temperature of electrolyte, applied voltage, stirring rate, electrolyte age, the specimen material and more will affect the final result.

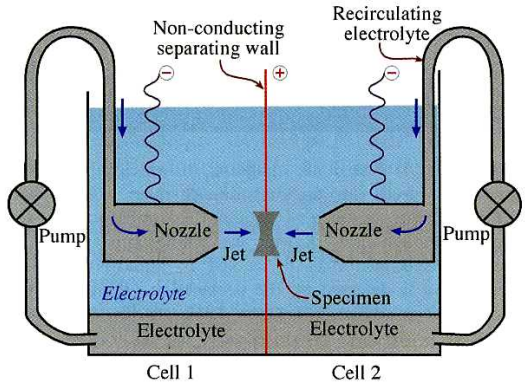

Figure 3.10: ***A schematic overview of a twin-jet electropolisher. [22].***

After the electropolishing the specimens were studied in a light microscope to determine which were best suited for further study in the TEM. Fig. 3.11 shows one sample with a promising hole. Only 5–10 of 20 specimens had holes that would be of interest for use in the TEM.

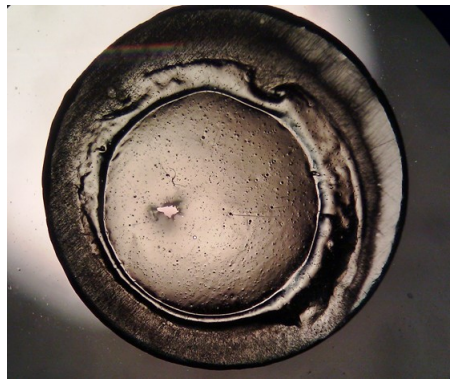

Figure 3.11: ***Picture of an electropolished TEM specimen. The shape and size of the hole(s) vary greatly between specimens.***

3.8 The Electron Microscopes

3.8.1 TEM

The TEM used in this experiment was a Philips CM30 microscope with a Gatan model 601 parallel electron energy loss spectrometer (PEELS) with EL/P software. It is shown in Fig. 3.12. All the work on the CM30 was done at 150 kV and the pictures were taken using negatives.

Figure 3.12: ***Picture of the CM30 used. The column, with the screen below, is left to the blue thermos.***

3.8.2 STEM

An JEOL 2010F, with an acceleration voltage of 200 kV, was used to get HAADF-STEM images of the precipitates, and an Oxford Instruments EDX detector was used to do the spectroscopy. The 2010F can be seen in Fig. 3.13

Before insertion in the JEOL 2010F, the specimen were cleaned using a Model 1020 Fischione plasma cleaner for 10 minutes to remove surface contaminations.

3.9 Microstructure Quantification

Quantity, size and length of precipitates were found using a MATLAB script [23]. The script worked by identifying the size, length and number of coloured areas in an image. The precipitates were coloured manually using Adobe Photoshop Elements. One TEM image would be coloured multiple times as precipitate numbers and lengths were found separately.

The precipitate density, ρ is defined by the following formula:

$$\rho = \frac{N}{V} = \frac{N}{t \cdot A} = \frac{N}{t \cdot \frac{A'}{M^2}} \tag{3.3}$$

Where N is the number of precipitates, V is the volume of the specimen in the TEM image, t is the thickness of the specimen, A is the real area, A' is the area of the TEM negative and M is the magnification.

In order to observe the specimen along the $\langle 100 \rangle_{\mathrm{Al}}$ direction, it was often necessary to tilt the specimen. This complicates calculation of the volume and the precipitate lengths. Fig. 3.14(b) shows how needles observed in the TEM image will be cut. As the tilt of the sample increases, so will the error.

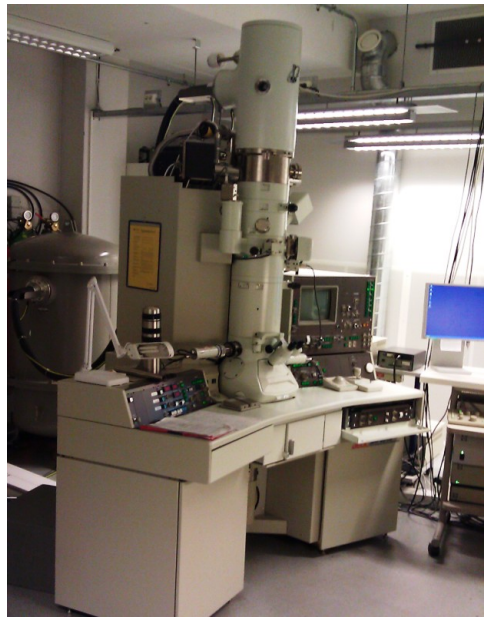

Figure 3.13: ***Picture of the JEOL 2010F used for STEM.***

3.9.1 Precipitate Length

The length of the precipitates is found by measuring the needles along the $[100]_{\mathrm{Al}}$ and $[010]_{\mathrm{Al}}$ directions. The $\langle 100\rangle_{\mathrm{Al}}$ zone axis will rarely be normal to the specimen surface and some of the precipitates will be cut by the tilted surface of the specimen. It is possible to take this into account and a estimated precipitate length can be found by [24]:

$$\langle l\rangle = \frac{\langle l\rangle_m}{1 - \frac{\langle l\rangle_m}{t}\cdot\cos(\theta)\cdot\tan(\Phi)}, \tag{3.4}$$

where $\langle l\rangle_m$ is the average measured precipitate length for an image, θ is the tilt of the $[100]_{\mathrm{Al}}$ and $[010]_{\mathrm{Al}}$ directions relative to the surface and Φ is the tilt of the specimen needed to get the $\langle 100\rangle_{\mathrm{Al}}$ zone. The holder used in the CM30 can be tilted in two directions orthogonal to the sample, by the angles α_1 and α_2, which means that $\Phi = \cos^{-1}(\cos(\alpha_1)\cdot\cos(\alpha_1))$.

The relative error of the length estimate is given by [24]:

$$\frac{\Delta\langle l\rangle'}{\langle l\rangle} = \frac{\langle l\rangle_m}{t}\cdot\cos(\theta)\cdot\tan(\Phi). \tag{3.5}$$

At $\theta = 45°$ needles in both direction are cut similarly and this can be assumed for low values of Φ. In this project no Φ greater than $10°$ was used and $\theta = 45°$ can safely be assumed.

There is also an error in the measuring of the precipitate length in itself and the total error in precipitate length for one TEM image will be these two errors

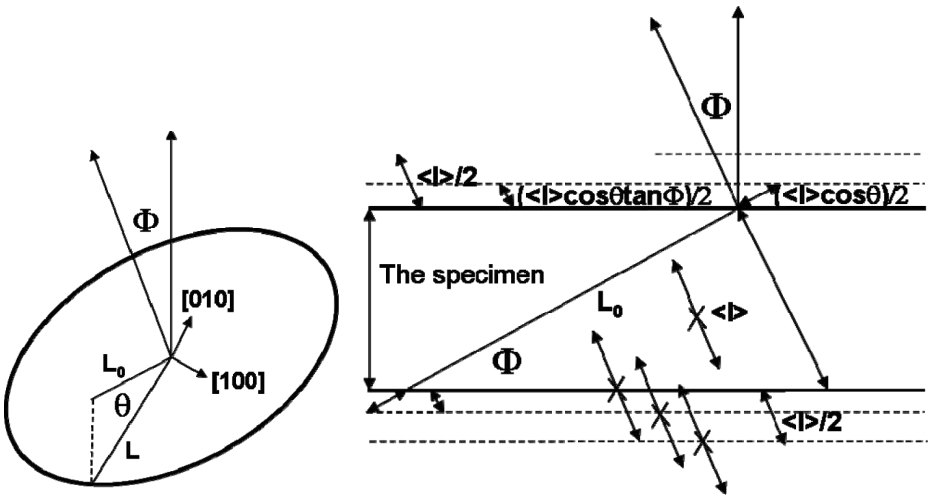

(a) (b)

Figure 3.14: ***The specimen surface and the plane formed by the*** $[100]_{Al}$ ***and*** $[010]_{Al}$ ***directions is tilted an angle*** Φ ***with respect to each other.*** θ ***describes how the*** $[100]_{Al}$ ***and*** $[010]_{Al}$ ***directions themselves are tilted relative to the surface (*** $\theta = 0^\circ$ ***means that needles along one direction is not cut, while the needles along the other direction are cut maximally).*** L ***is the length of a structure inside the specimen and*** L_0 ***is the observed projection of*** L***. [24]***

combined:

$$\Delta\langle l\rangle = \langle l\rangle \cdot \sqrt{\left(\frac{\Delta\langle l\rangle'}{\langle l\rangle}\right)^2 + \left(\frac{s_l}{\langle l\rangle_m}\right)^2}, \tag{3.6}$$

where s_l is the SEM for the measurement of the precipitate length, as given by equation 3.1.

The mean of $\Delta\langle l\rangle$ from all the images is calculated and added with the SEM of the $\langle l\rangle$ for the images to give the total error of the precipitate length.

3.9.2 Number Density

When the number density is high it will be hard to get a clear view of the precipitates growing in the $[100]_{\mathrm{Al}}$ and $[010]_{\mathrm{Al}}$ directions. It is possible to get the density by only counting the precipitates along the $[001]_{\mathrm{Al}}$ direction (seen as dots in Fig 3.15) since the needles are randomly oriented along the $\langle 100\rangle_{\mathrm{Al}}$ direction. The number of precipitates counted is then multiplied by 3 to give the total number of precipitates in the image. This gives the following equation for the precipitate density [24]:

$$\rho = \frac{3N}{A \cdot (t + \langle l\rangle)}. \tag{3.7}$$

Which have an error given by [24]:

$$\Delta\rho = \rho \cdot \sqrt{\left(\frac{\Delta V}{V}\right)^2 + \frac{\left(\frac{\Delta\langle l\rangle}{\langle l\rangle}\right)^2 + \left(\frac{\Delta t}{t}\right)^2}{\left(1 + \frac{t}{\langle l\rangle}\right)^2}}, \tag{3.8}$$

where

$$\frac{\Delta V}{V} = \sqrt{\left(\frac{\Delta A'}{A'}\right)^2 + 4 \cdot \left(\frac{\Delta M}{M}\right)^2 + \left(\frac{\Delta t}{t}\right)^2}. \tag{3.9}$$

$\frac{\Delta A'}{A'} \approx 1\%$ [24], $\frac{\Delta M}{M} \approx 5\%$ [22] and $\frac{\Delta t}{t} \approx 10\%$ [24] gives:

$$\frac{\Delta V}{V} \approx 15\%. \tag{3.10}$$

The average of $\Delta\rho$ from the different TEM images added to the *SEM* for the number density of all the images.

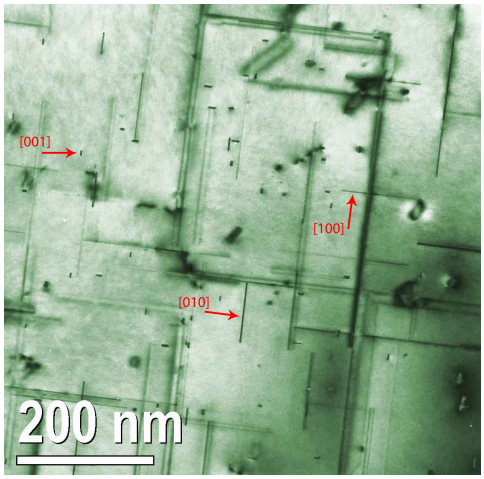

Figure 3.15: ***The different directions of the needle-like precipitates. This is the KK30 alloy after 24 hours of over-ageing. Image taken along the*** $[001]_{Al}$ ***direction***

3.9.3 Volume Fraction

The volume fraction, VF, is given by:

$$VF = \rho \cdot \langle CS\rangle \cdot \langle l\rangle, \tag{3.11}$$

where $\langle CS\rangle$ is the average cross section of the precipitates.

The upper and lower relative error of VF is given by[24]:

$$\frac{\Delta VF}{VF}_{\text{upper}} = \sqrt{\left(\frac{\Delta\langle CS\rangle}{\langle CS\rangle}\right)^2 + \left(\frac{\Delta\langle l\rangle}{\langle l\rangle}\right)^2} \tag{3.12}$$

$$\frac{\Delta VF}{VF}_{\text{lower}} = \sqrt{\left(\frac{\Delta\langle CS\rangle}{\langle CS\rangle}\right)^2 + \left(\frac{\Delta V}{V}\right)^2 + \frac{\left(\frac{\Delta\langle l\rangle}{\langle l\rangle}\right)^2 + \left(\frac{\Delta t}{t}\right)^2}{\left(1+\frac{t}{\langle l\rangle}\right)^2}} \tag{3.13}$$

$\Delta\langle CS\rangle$ is the SEM of the cross section.

The volume fraction and error is calculated for each of the different precipitates found. The total volume fraction is the mean for all the precipitates, while the errors are added using the following equation:

$$\Delta VF = \sqrt{(\Delta VF_1)^2 + \Delta(VF_2)^2 + \ldots + \Delta(VF_n)^2}, \tag{3.14}$$

where n is the total number of precipitate types.

Chapter 4

Results and Discussion

Data from the hardness measurements can be found in Appendix C and the TEM images used for the microstrucure quantification can be found in Appendix D.

4.1 Hardness Measurements

The results of the hardness tests made during the over-ageing at 250°C can be seen in Fig. 4.1.

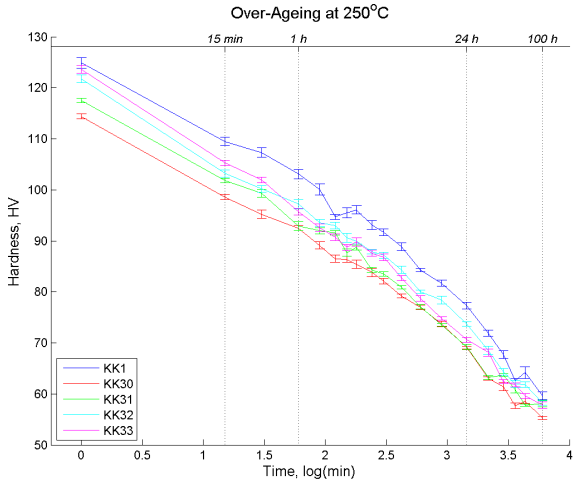

Figure 4.1: ***Hardness measurements for KK1 and the KK3x series over-aged at 250° C. HV5 was used up until the 24 hour mark, and HV1 was used from the 24 hour mark. Data from table C.1 and C.2.***

It is clear that the over-ageing of the alloys starts right away, and that peak hardness is lost instantly.

The difference in hardness between the KK3x alloys is small, and there is some overlap of hardness, and errors, during the over-ageing.

The KK32 alloy has the highest hardness during the over-ageing, even though it has neither the highest or lowest Ge-content. It has been proposed that this could be due to an error in the alloy composition [25], but it has not been possible to test the Ge-content of the alloys. KK33 has the second highest hardness and almost overlap with the KK32, while KK30 and KK31 more or less overlap over the duration of the over-ageing.

In Fig. 4.2 only the KK30, KK33 and KK1 alloy are shown. Here it seems to be a clear difference based on the Ge-content of the alloys. Contrary to the hypothesis that the germanium would increase the hardness, it seems like there is a negative correlation between the hardness and the Ge-content. The KK30 alloy, with the most germanium, consistently shows a lower hardness value than the KK33 and KK1 alloys, which have little and no Ge-content. The difference is small, but it is constant during the over-ageing.

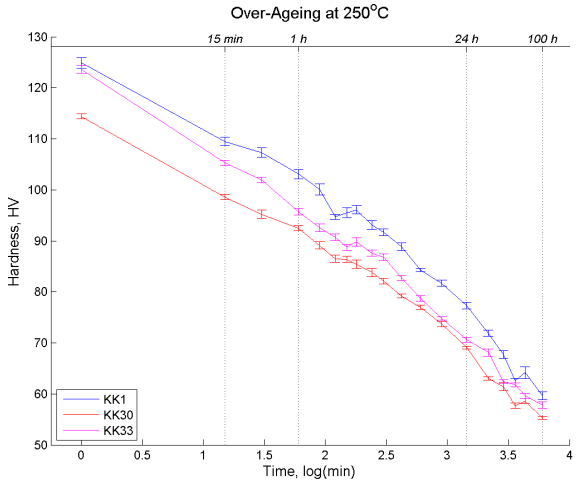

Figure 4.2: ***Comparison of the KK1 (0 at.% Ge), KK30 (0.037 at.% Ge) and KK33 (0.002 at.% Ge) alloy over-aged at 250°C. HV5 was used up until the 24 hour mark, and HV1 was used from the 24 hour mark. Data from table C.1 and C.2***

4.1.1 200°C

Fig 4.3 shows the same alloys over-aged at 200°C. The data on KK3x at 200°C is from unpublished SINTEF work.

It is observed that also here the KK32 alloy shows a higher hardness than for any of the other KK3x alloys, but is very similar to the KK33 alloy.

It can be seen that the T6 heat treatment did not result in the Ge-containing alloys possessing a peak hardness at the start of the over-ageing, but this was

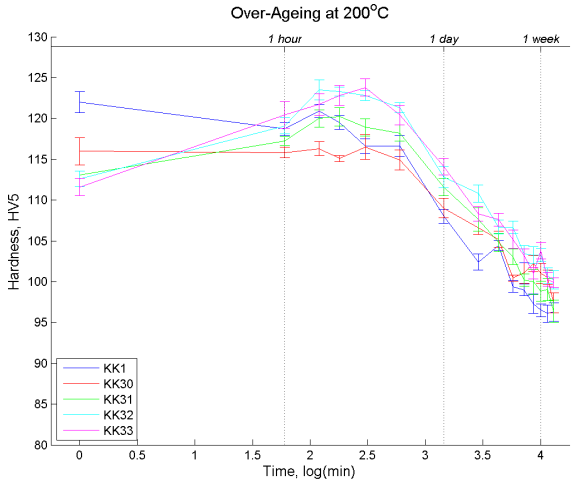

Figure 4.3: ***Hardness measurements for the KK3x series over-aged at 200° C. Data on KK1 from [26] and KK3x values from unpublished SINTEF work.***

achieved after a couple of hours at 200°C. This is due to a difference in composition that will affect the speed the artificial ageing during the heat treatment. This will affect the comparison of KK1 and the KK3x series, as the KK1 is at a later stage in the over-ageing. However, the peak is reached relatively fast by the KK3x alloys, and there it should not give a large error later into the over-ageing.

Up until two days of over-ageing at 200°C, there seems to be a similar negative correlation between hardness and Ge-content of the KK3x alloys as with 250°C. After one week of over-ageing, the overlap of the hardness curves increases and it is difficult to say anything for certain. However, the KK3x alloys have a higher hardness than the KK1 alloy with no Ge-content. This might be another indication that there is a problem with the actual Ge-content of the KK3x series.

In Fig. 4.4 only the KK1, KK30 and KK33 is compared, and the difference between the KK30 and KK33 is clearer.

Hardness Discussion

The reason that the KK3x have a greater hardness than the KK1 for over-ageing at 200°C and a lower hardness for over-ageing at 250°C could be a consequence of a too rapid over-ageing at 250°C. It is possible that the alloys overage so fast that it is not realistic to compare the development of the alloys. The fact that the KK1 is more over-aged than the KK3x series should only have an effect early in the over-ageing process.

It appears that for both over-ageing at 200°C and 250°C, the difference in hardness between the four Ge-containing alloys decreases as the over-ageing progresses. This could mean that they all possess a similar equilibrium state where the germanium contributes less to the microstructure.

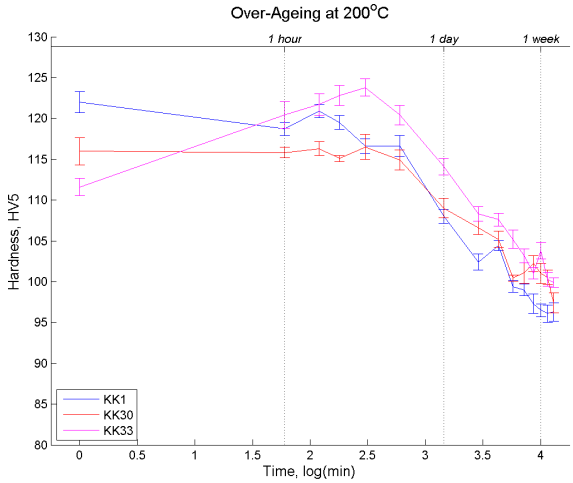

Figure 4.4: ***Comparison of the hardness of KK1 (0 at% Ge), KK30 (0.037 at% Ge) and KK33 (0.002 at% Ge) alloy during over-ageing at 200° C. Data on KK1 from [26] and KK3x values from unpublished SINTEF work.***

The initial hardness of the KK3x series at 200°C and 250°C is not the same. This could come from differences in the way the hardness was tested, the calibration of the hardness testing machines or some small variation in the heat-treatment.

4.2 Microstructure

4.2.1 TEM

TEM specimens were made from the KK30 and KK33 alloy after 24 and 100 hours of over-ageing at 250°C. The 24 hour mark was chosen as it was more or less in the middle of the hardness curves, while the 100 hour mark was at the end.

After 100 hour the amount of dislocations in the specimens were so great that it was necessary to tilt the sample away from the $\langle 100 \rangle_{\mathrm{Al}}$ axis by a few degrees in order to see anything. This made it hard to get good images of the precipitates and there is a large difference between the images. Fig. 4.5 gives one example of how tilting away from the $\langle 100 \rangle_{\mathrm{Al}}$ axis will help the image. In this case the amount of tilting was small, and in most of the cases several of degrees were needed to get a usable image.

Fig. 4.6 shows four TEM images of the microstructure for KK30 and KK33 at 24 and 100 hours. The rest of the images used for the microstructure analysis are found in Appendix D. The TEM images show no clear visible difference between the KK30 and KK33 alloys.

It is assumed that only the L precipitates are needles, while all the other precipitates are lath-shaped. This means that the precipitate density of the Q′ phase

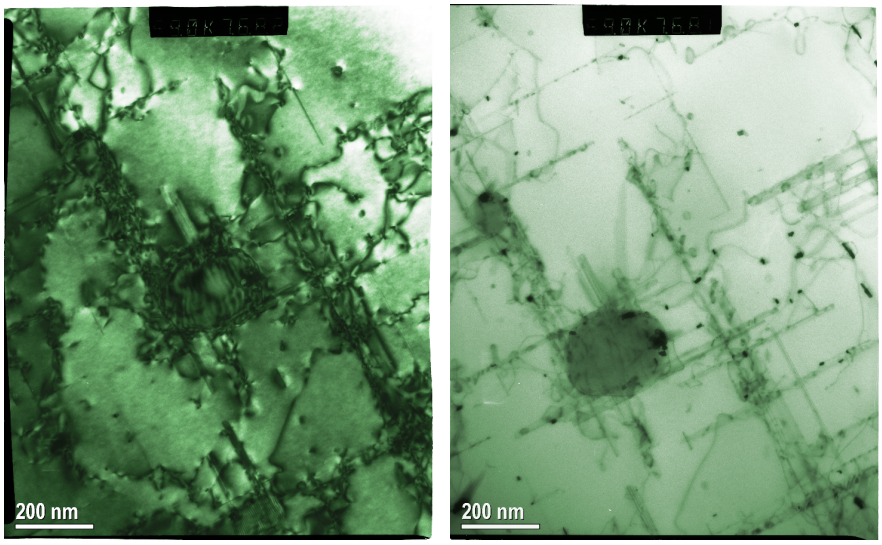

(a) $\langle 100 \rangle_{\mathrm{Al}}$ (b) 1° away from $\langle 100 \rangle_{\mathrm{Al}}$

Figure 4.5: ***a) Image of a specimen seen along the*** $\langle 100 \rangle_{Al}$ ***zone axis. b) Image of the same position (shifted down a bit) tilted to get a good picture. Only a small amount of tilt was needed for getting a good image in this case. Image of KK30 at 100h.***

and the remaining could both erroneous, as there could be a difference in their lengths. The L is distinguished from the Q′ precipitates due to the orientation of their cross-section, as it is not possible to see any other difference between these two precipitates in a TEM image. Fig. 4.7 points out the precipitates and the needles and laths. The Q′ phase's cross-section is not always oriented along the $\langle 510 \rangle_{\mathrm{Al}}$ and some Q′ precipitates will be identified as L. This will be discussed later.

In the TEM images it is not possible to distinguish between Q′ and Q precipitates and this will give an error in the data on Q′. All precipitates that were not identified as L or Q′ were placed in the same category called *remaining*.

The lath-length after 100 hours becomes so great that equation 3.4 and 3.5 breaks down. Their length is almost 10 times the thickness of the sample which means that most likely every lath has been cut and the assumptions used to get equation 3.4 no longer applies. For the 100h specimens the lath-length is not calculated using equation 3.4 and 3.5, but is the measured average length and the error is the *SEM* of the measured lengths and the average length for all the images.

Table 4.1 shows the data on the precipitates found from the TEM images, and table 4.2 shows an average of the precipitates. It was difficult to get many images of cross-sections for all of the precipitates, and there will be a larger error in the

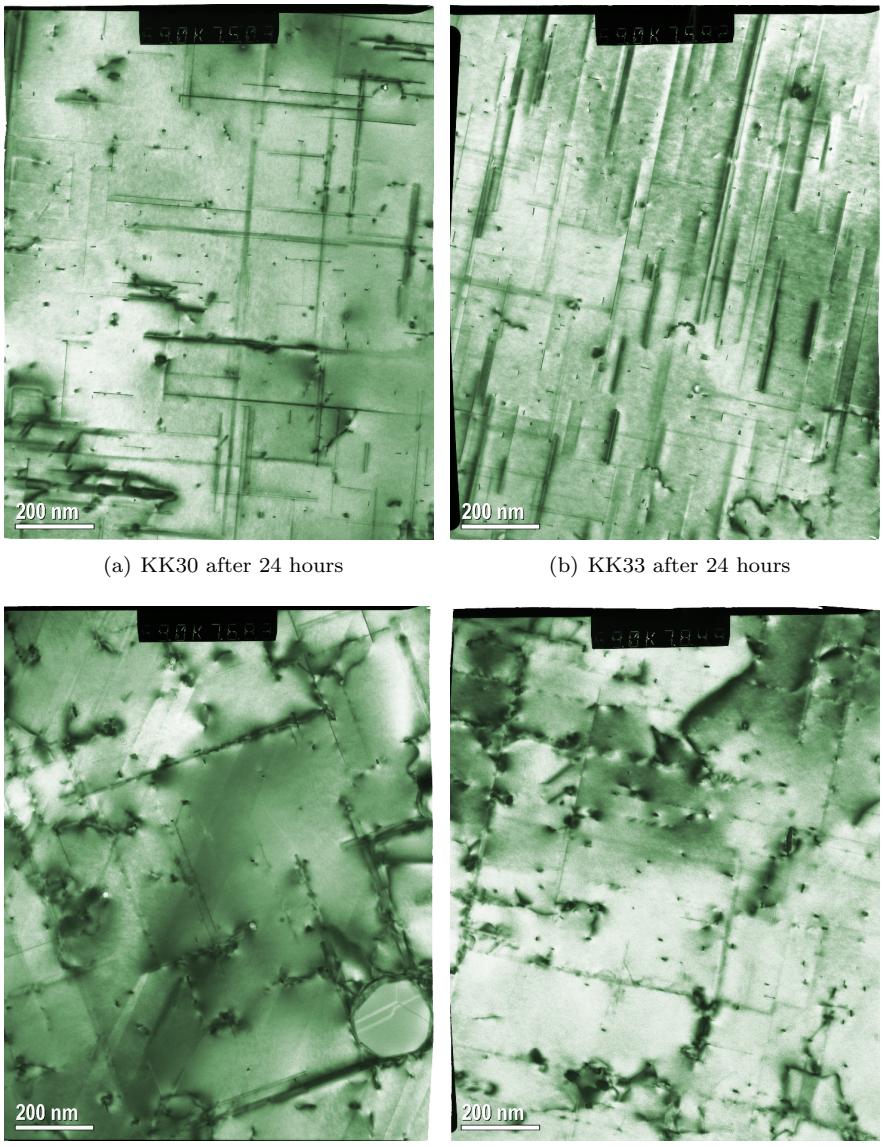

(a) KK30 after 24 hours

(b) KK33 after 24 hours

(c) KK30 after 100 hours

(d) KK33 after 100 hours

Figure 4.6: ***TEM images of the two alloys after 24 and 100 hours at 250°C.***

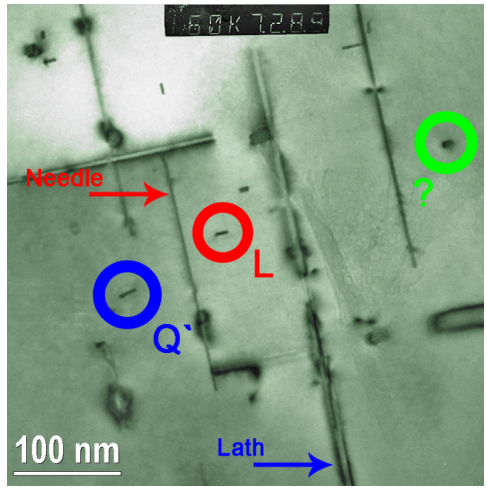

Figure 4.7: ***The L and Q′ precipitates and the needles and laths. KK30 after 24 hours.***

cross-section than what the table indicates.

At 24 hours there is little difference between the KK30 and KK33 alloys, with both containing mainly L precipitates, with some Q′ and other phases. The needles are about half the length of the laths.

After 100 hours the total number density has decreased to a third compared to 24h. There are fewer precipitates, but they are longer and have larger cross-sections. The volume fraction has also increased, as more of the alloy elements have been absorbed into the precipitates. Looking at table 3.1 it can be seen that the total fraction of solute elements should be around 2%, however, the rest of the elements have most likely dispersed into grain boundaries or dispersoids, which are not studied in this thesis.

It appears that there is a small difference between the two alloys at 100h, with more L precipitates and longer laths in the KK33 alloy, but this can easily be a result of the difficulties in seeing the difference between the precipitates, and the needles and laths at 100 hours. The errors are overlapping for all of the values as well, so it is not possible to conclude that there is a difference in the microstructure of the two alloys.

TEM imaging is qualitative not quantitative, and images taken do not necessarily represent the sample. Only 1–3 specimens for each condition was used for TEM, and only 2–3 grains on each specimen were taken images of. Pictures were taken on "good" positions with clearly visible precipitates, and this may not be representative for the sample as a whole.

Table 4.1: ***Microstructure quantification of KK30 and KK33 after 24 and 100 hours at 250°C. At 100h the lath-length is not calculated, but is the average measured length. The L phase observed after 100 hours is most likely Q′ precipitates.***

Precipitate	**Number density** (μm^{-3})	**Precipitate length** (nm)	**Cross section** (nm^2)
KK30 (24h)			
L	895.29±237.20	199.11±41.10	27.34±2.93
Q′	53.66±27.22	488.44±218.84	23.06±9.00
Remaining	37.74±19.95	— " —	38.08±7.00
KK33 (24h)			
L	840.71±210.47	192.44±33.78	33.63±2.92
Q′	49.04±21.54	362.60±74.73	36.24±5.66
Remaining	35.61±15.65	— " —	53.25±12.82
KK30 (100h)			
L	139.40±66.29	337.41±171.31	40.12±4.18
Q′	39.37±19.43	543.19±129.40	40.24±5.90
Remaining	50.17±17.55	— " —	207.31±49.44
KK33 (100h)			
L	240.54±101.75	334.58±137.77	51.31±5.77
Q′	44.15±14.92	759.95±200.90	42.83±4.09
Remaining	53.11±22.78	— " —	180.45±45.17

Table 4.2: ***Average microstructure in KK30 and KK33 at 250°C. Values based on table 4.1.***

Alloy	**Number density** (μm^{-3})	**Volume fraction** (%)	**Upper** ΔVF (%)	**Lower** ΔVF (%)
24h				
KK30	986.69±238.21	0.618	0.124	0.094
KK33	925.36±197.04	0.677	0.110	0.094
100h				
KK30	228.95± 78.12	0.840	0.215	0.165
KK33	337.80±107.47	1.285	0.321	0.243

4.2.2 HAADF-STEM

It is not possible to get much information on the precipitates using TEM with the CM30, so HAADF-STEM images were taken on some precipitates in the KK33 alloy after 100 hours of over-ageing at 250°C. Just one specimen was studied.

HAADF-STEM images have Z-contrast which allow for discriminating between atomic columns with different atomic numbers. Cu-columns are very easy to see as they are much brighter than the Si columns. In order to reduce noise, all features smaller than 4 Å has been filtered out of the STEM images using image processing.

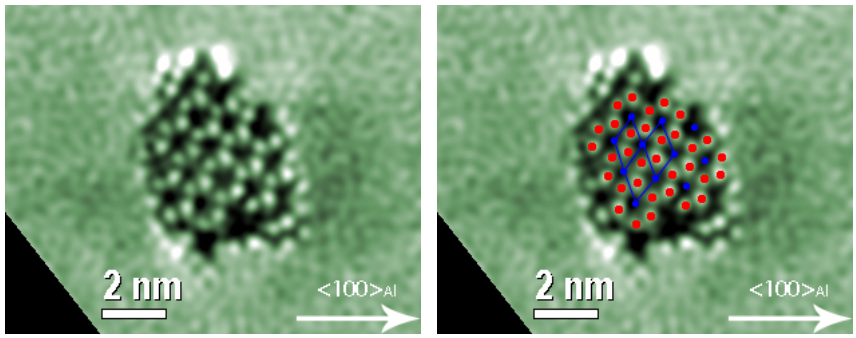

(a) (b)

Figure 4.8: ***The atomic structure of the Q′ phase. Red dots are the Cu columns and the blue represent the Si columns (which can not be seen in these images). Images taken by Calin D. Marioara.***

The majority of the precipitates had a hexagonal structure that is representative for the Q′ phase. Fig. 4.8 shows the structure that defines the Q′ phase, a hexagonal Cu structure with an underlying Si network. There was a large variation in the shape of these precipitates as seen in Fig 4.9.

As seen in Fig. 4.9 the Q′ precipitates do not always have their cross-section oriented in the $\langle 510 \rangle_{\mathrm{Al}}$ direction. Since no L precipitates were observed with HAADF-STEM, it can be assumed that most of the precipitates defined as L in table 4.1 were actually Q′ precipitates. This means that alloys are fully over-aged after 100 hours, as there are no longer any strengthening phases present.

It is possible that some of the Q′ precipitates observed were actually Q precipitates, as there is not a large structural difference between them. This can be assumed because the large amount of over-ageing suggests that some equilibrium phases should have shown up. There is also a size difference in the precipitates that could suggest that the small precipitates, with a hexagonal structure, are Q′ while the larger ones are Q.

Some of the precipitates had both a hexagonal structure and a disordered structure, as seen in Fig. 4.10. It is not clear what these precipitates are.

Some large unknown precipitates were also observed, with one example in Fig. 4.11. At this time nothing is known about them.

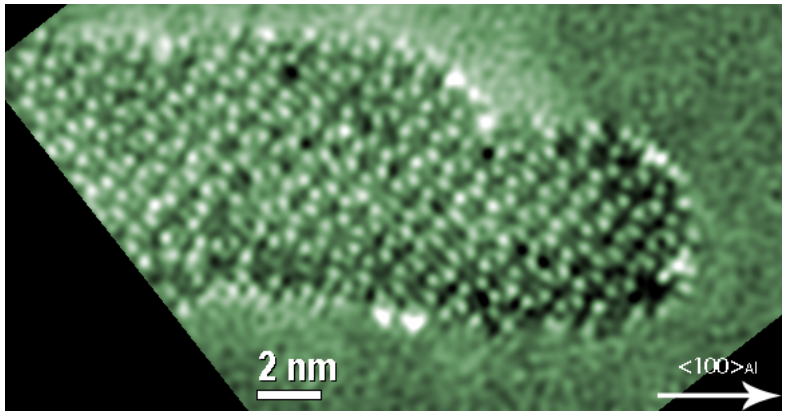

(a)

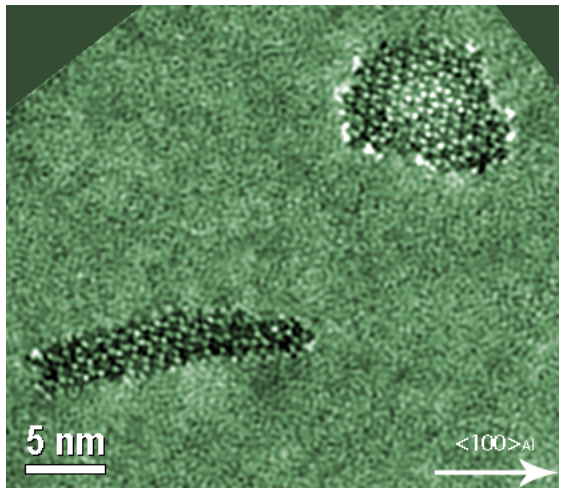

(b)

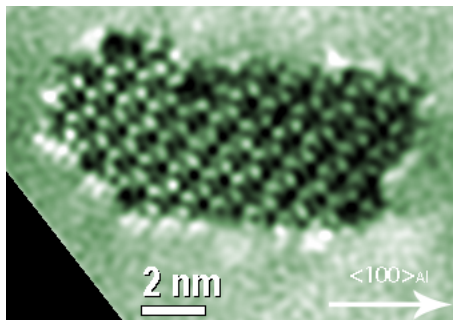

(c)

Figure 4.9: ***Differently shaped Q′ precipitates. Images taken by Calin D. Marioara.***

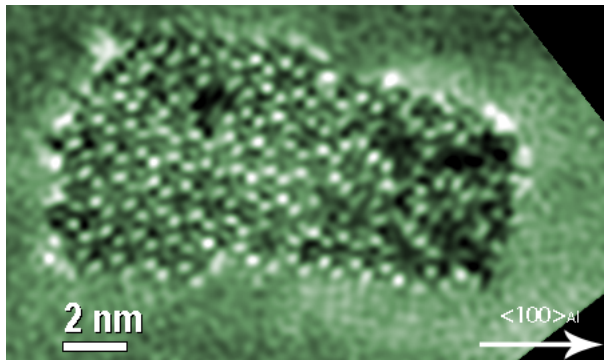

(a)

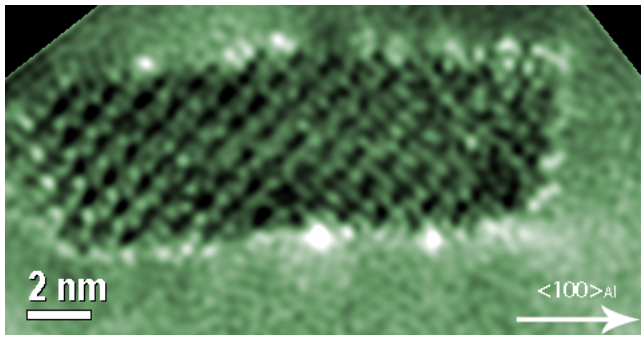

(b)

Figure 4.10: ***Partly disordered precipitates with both hexagonal structure and disorder. Images taken by Calin D. Marioara.***

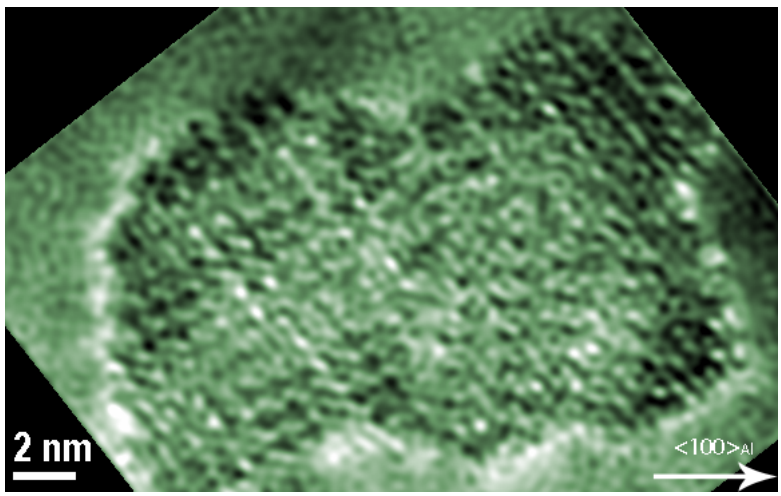

Figure 4.11: ***Unknown precipitate. Image taken by Calin D. Marioara.***

A difference in the hexagonal structure was observed for some of the precipitates. While the majority of the Q′ precipitates had a hexagonal structure of bright Cu atoms, for some there was a regular difference in the brightness. Fig. 4.12 shows the rectangle of brighter Cu columns present in the hexagonal structure. This could be a result of some unknown superstructure in the column, with more Cu atoms in the rectangle.

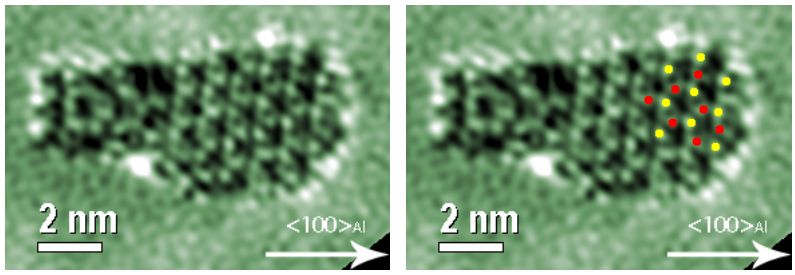

(a) (b)

Figure 4.12: ***Triangular structure within the hexagonal structure. Yellow dots are brighter columns and red are the duller columns. Images taken by Calin D. Marioara.***

In order to study the presence of germanium, EDX spectroscopy was done on some precipitates. Fig. 4.13 shows two precipitates studied and their spectrum. The presence of aluminium observed could come both from the aluminium matrix and the precipitates. These spectra are more or less representative for all the precipitates studied, which showed different ratios of silicon and magnesium and a similar amount of copper. No Ge-content was detected in any of the precipitates studied. KK33 was supposed to have the least amount of Ge-content, however, it was expected that there would be some germanium present in the precipitates. There is a presence of oxygen in the spectra, due to a oxide layer on the specimen, originating either from the specimen preparation or from some etching on the surface.

For more or less all of the precipitates studied an enrichment at the interfaces of the precipitates were observed, with much brighter atomic columns at the edge of the precipitates compared to the center. It was not possible to determine what the cause of this could be. Two possible explanations could be a larger presence of copper on the interface than in the precipitate (due to vacancies in the Cu-columns within the precipitates), or a presence of germanium at the interface. The EDX is not accurate enough to determine the atomic structure of single atomic columns, and an attempt to do EDX the edge of a precipitate showed no germanium.

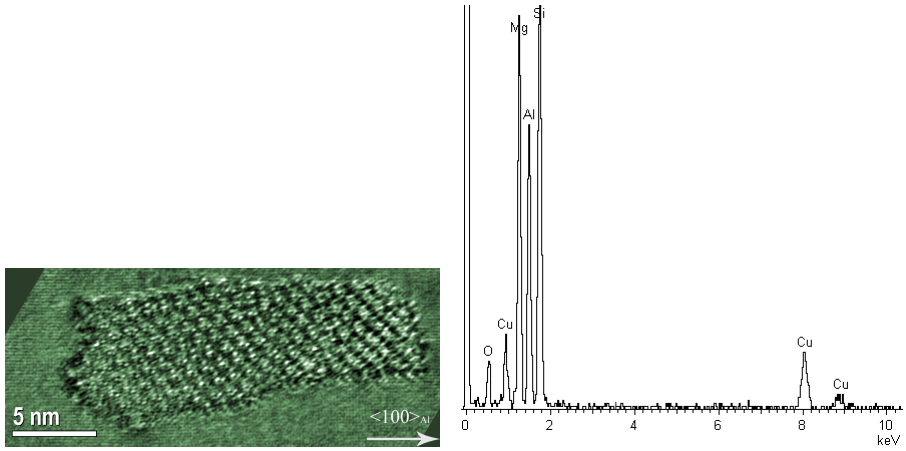

(a) Precipitate (b) EDX spectrum

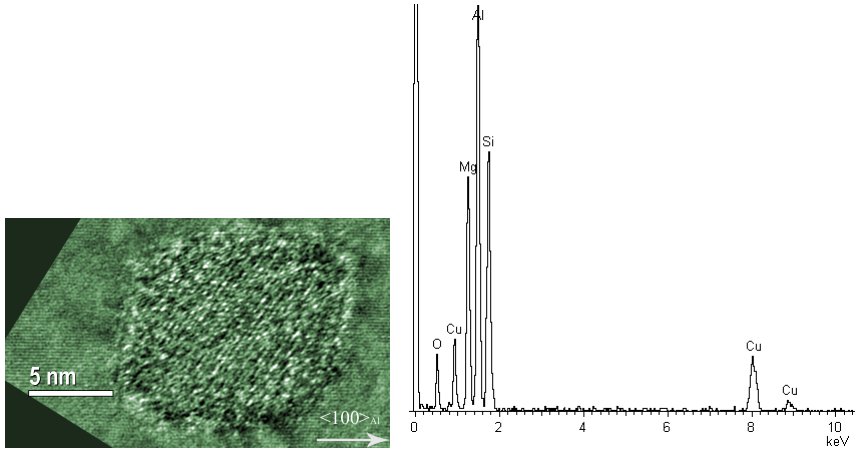

(c) Precipitate (d) EDX spectrum

Figure 4.13: ***The spectra and high resolution TEM images two precipitate. Structures smaller than 2 Å was filtered out of the images. The other spectra taken were similar to these two. Images taken by Calin D. Marioara.***

4.3 Compared to Old Data

In a paper from 2007 by Calin Marioara et al. two Al-Mg-Si-Cu alloys were over-aged at 260°C [16]. These alloys had a different composition of silicon and magnesium than the KK3x alloys, but had a similar Cu-content[1].

After 3 hours at 260°C there were similarities in hardness and microstructure with the KK3x alloys at 100 hours. They had a greater number density ($\sim$ 400–500 μm^{-3}) and volume fraction ($\sim$ 2%) than the KK3x alloys, and had a similar precipitate length and cross-section (in average). Their hardness after 3 hours was $\sim$ 70 HV compared to the less than 60 HV of the KK3x series at 100 hours.

4.4 Effect of Ge-Content

The understanding of the effect of Ge-content on Al-Mg-Si-Cu alloys came from the project-work of Jan Fredrik Helgaker in the autumn of 2009 [4]. Appendix A notes that the results in this work was erroneous. For some reason the hardness curves of the Ge-free alloys in the work were the correct ones, while the Ge-containing alloys showed a too small decrease of hardness during the over-ageing, as defined by Appendix A. This meant that the effect of germanium on the hardness was exaggerated, and that the small effect observed here at 200°C (compared to the KK1 alloy) is not too surprising.

At 200°C it is the KK24 alloy (0.05 at.%) that has the superior hardness compared to other KK alloys [26], and the Ge-content in the KK3x alloys may be too small to have a large effect.

4.5 Further Work

- The 100h over-aged TEM samples were too over-aged for good microstructure and precipitate determination. Another TEM sample between T6 and 24h, and one after 24h would be needed to get a proper understanding of the precipitate development in the alloys.
- More of the KK3x alloys should be tested with STEM in order to see if there is a difference in the microstructure of the alloys.
- The alloy composition needs to be tested to determine if the Ge-content is correct.
- The T6 heat treatment used on the KK3x alloys do not produce a peak hardness in the alloys. If further studies are to be made on these alloys the correct T6 heat treatment should be found.

[1] 0.72/0.57 at.% Si, 0.56/0.72 at.% Mg and 0.13 at.% Cu

Chapter 5

Conclusion

- KK3x series has a higher hardness than the KK1 alloy, with no Ge-content, during over-ageing at 200°C, while they have a lower when over-aged at 250°C. This could be because 250°C is a too high temperature which causes a far too rapid over-ageing.
- At 250°C the over-ageing progresses fast and within 100 hours the alloys are fully transformed (no strengthening precipitates present).
- KK32 seems to be the hardest alloy even though it has neither the most or the least amount of Ge-content, however, there could be a problem with the alloy compositions.
- Within the KK3x series there seem to be a negative hardness effect from the germanium for both temperatures (ignoring the KK32 alloy).
- The 200°C series seem to indicate that the Ge-content of the KK3x alloys is too small to get a large hardness increase.
- The precipitate quantification showed little difference in microstructure between the KK30 and KK33 alloys after 24 and 100 hours.
- In the KK33 alloy after 100 hours of over-ageing at 250°C most of the precipitates studied with STEM was Q′ (some possibly Q), and it was not observed any germanium in any of the precipitates.

Appendix A

Discrepancy Between Old and New Data

This master thesis is a continuation of a project-work done in the autumn of 2011 [27]. During the project-work inconsistencies were found between old and the new hardness measurements for the alloys studied.

It was discovered later that Jan Fredrik Helgaker had discovered this discrepancy in autumn 2009 when two similar alloys showed a great difference between the hardness curves [4]. It was then assumed that the reason was a wrong alloy composition, but this was tested and was ruled out as a cause. No further investigation was made until the discrepancy was rediscovered during the project-work in 2011.

The project-work tried to find the source of the differences by changing various parameters in the experiments and testing the hardness during over-ageing. Two examples of the difference between the old and the new results are shown in Fig. A.1 to give some indication of the size of the inconsistency.

Some of the parameters that were tested were: Multiple old and new T6 heat treatments, different alloys, different size on samples, different student doing the experiment and different hardness testing machines. All the tests gave similar results that deviated from the old measurements. There were no clear conclusions in the project-work, therefore more experiments were conducted at the start of this master thesis.

Two things that were mentioned in the project-work as possible sources for the difference was a problem with the type of sand-bath or some unnoticed difference in temperature between the old and new experiments.

A.1 The 250°C Bath Used

It was decided to do the over-ageing with something different than a sand-bath. The only baths at NTNU that works in the 250°C range are sand-baths, so the over-ageing was tested out at Hydro Aluminium Sunndal. A salt-bath, with a

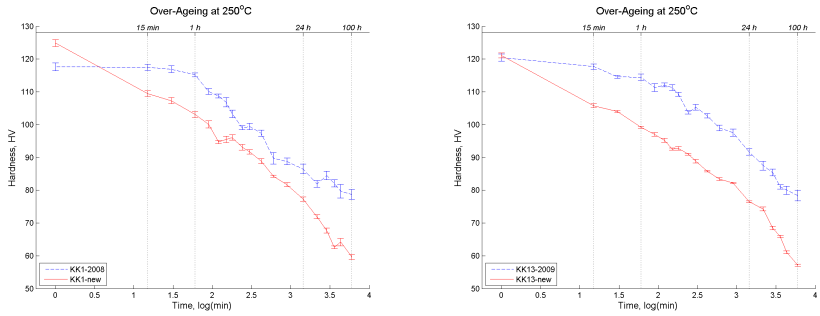

(a) KK1 (b) KK13

Figure A.1: ***Comparison of old and new hardness data for two Al-Mg-Si-Cu alloys. Data from [27] and table C.2.***

temperature range of 150–350°C, and a Matsuzawa DVK-1 hardness tester was used.

In Fig. A.2 it is shown that it was the new results that were replicated at Sunndal.

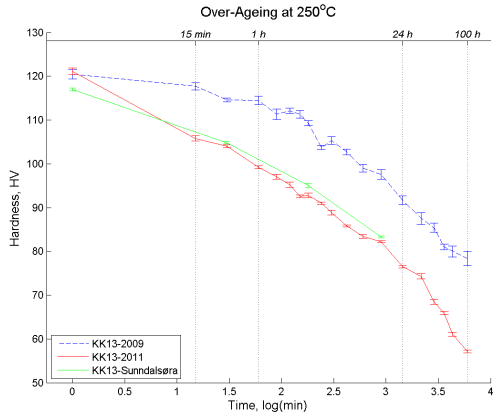

Figure A.2: ***One of the alloys tested at Sunndal compared with two identical alloys tested at NTNU in 2009 and during the project-work in 2011. Data from [27] and table C.4.***

A.2 Different Temperature

Due to the shape of the hardness curves it was thought that the difference could come from a different temperature being used in the old experiments.

A comparison of different over-ageing temperatures can be seen in Fig. A.3. The new experiment at 220°C is closer to the old 250°C experiment than the new 250°C experiment. If the problem was a too low temperature in the old experiments, then the graphs suggest that old temperature must have been between 220°C and 230°C.

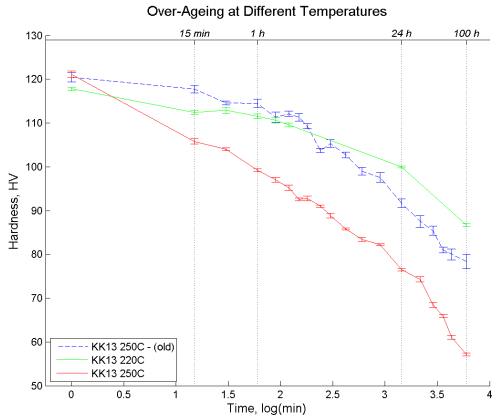

Figure A.3: ***The KK13 alloy tested at different temperatures. Data from [27], [28] and table C.5***

Due to time constraints it has not been possible to experiment with different temperatures and confirm whether there was a specific erroneous temperature that was used in the old experiments.

How two different people over a period of two years [4, 28] did not notice the use of a wrong temperature is unknown. Especially since the temperature of the sand-bath was measured at least once [29].

A.3 Conclusion

Since the new shapes of the hardness curves were observed again at Sunndal it was concluded that it is the new data that is correct. The reason for the old results is still not understood, and while a too low temperature seems to be the reason for the old results, the reason for the wrong temperature is unknown.

Appendix B

Magnification Calibration

The strength of the magnetic lenses in a TEM is dependent on different factors that cannot all be controlled. This means that the magnification given by the TEM will differ from the actual magnification in the images. With no calibration the magnification is expected to have an error of ±10%, however, this can be reduced to ±5% with the proper calibration [22].

The correct magnification can be determined using the erroneous magnification given by the TEM and a specimen of known parameters. A thin carbon-film with a linear spacing of 0.463 μm was used for the calibration of the CM30 microscope. A TEM image of the specimen can be seen in Fig. B.1. The correct magnification is found by measuring a line on the image using a Gatan DigitalMicrograph script and counting the number of blocks the line traverses.

$$M_{real} = \frac{\text{Length on picture}}{\text{Length on specimen}}$$

$$= \frac{\frac{\text{Length of line}}{\text{Resolution of picture}}}{\#\text{blocks} \times \text{Length of block}}.$$

Two pictures were taken in total on each magnification, during either a series of increasing or decreasing magnifications, and four lines were measured on each image. The magnification in the 160k× image was too great and it was only possible to measure two lines.

To ensure consistency every TEM picture was taken at the eucentric height, which means adjusting the specimen so it lies perpendicular to the optical axis. At this position the image of the specimen will not move when the specimen is tilted around the axis of the holder.

All images in this report have been adjusted according to table B.1.

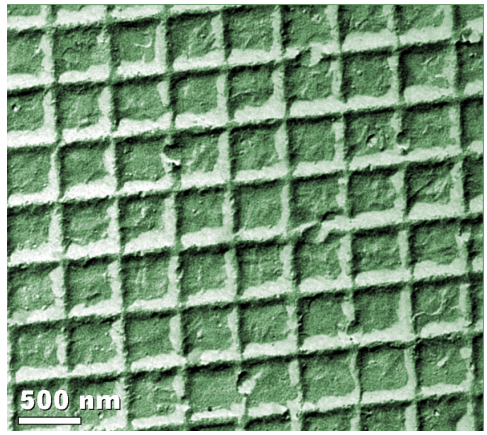

Figure B.1: ***TEM image of carbon-film grating taken with the CCD camera. (The CCD camera has a different correction factor than the negatives).***

Table B.1: ***Calibration factors for negatives from the CM30 at 150 kV. All but the 420k× and the 600k× calibrations were done by the author during the summer of 2011.***

Given magnification	Actual magnification	Correction factor
17 000	18 100±33	1.063
21 000	22 100±49	1.054
31 000	31 700±42	1.023
42 000	42 500±222	1.013
52 000	52 000±249	1.000
69 000	68 950±590	0.999
89 000	87 600±330	0.984
120 000	121 600±1 365	1.013
160 000	161 800±855	1.011
420 000	403 200	0.96
600 000	486 000	0.81

Appendix C

Tables

The results from the hardness test made during the master thesis.

It should be noted that the variation in the hardness measurements for some condition were sometimes greater than what the errors indicates, with a even distrubution of values ±10 HV from the mean.

Table C.1: ***Measured hardness for the KK3x alloys during over-ageing at 250° C.***

Time (h)	**KK30** HV5	**KK31** HV5	**KK32** HV5	**KK33** HV5
0.00	114.4 ± 0.45	117.5 ± 0.45	121.8 ± 0.79	123.6 ± 0.76
0.25	98.6 ± 0.52	101.8 ± 0.42	103.2 ± 0.71	105.3 ± 0.50
0.50	95.2 ± 0.81	99.3 ± 0.76	100.2 ± 0.63	101.9 ± 0.53
1.00	92.5 ± 0.52	92.9 ± 0.89	97.2 ± 0.93	95.7 ± 0.65
1.50	89.1 ± 0.69	92.0 ± 0.60	93.5 ± 0.72	92.6 ± 0.78
2.00	86.5 ± 0.73	91.6 ± 0.45	93.0 ± 0.70	90.7 ± 0.65
2.50	86.4 ± 0.60	87.7 ± 0.68	90.6 ± 0.88	88.7 ± 0.60
3	85.4 ± 0.79	88.7 ± 0.52	90.0 ± 0.61	89.8 ± 0.79
4	83.8 ± 0.81	84.3 ± 0.47	87.9 ± 0.41	87.6 ± 0.60
5	82.1 ± 0.55	83.5 ± 0.43	87.2 ± 0.59	86.8 ± 0.65
7	79.2 ± 0.39	80.9 ± 0.38	84.3 ± 0.70	82.7 ± 0.50
10	77.0 ± 0.42	77.1 ± 0.46	80.0 ± 0.33	78.7 ± 0.52
15	73.7 ± 0.54	73.5 ± 0.27	78.4 ± 0.72	74.8 ± 0.29
24	69.1 ± 0.28	69.2 ± 0.49	73.7 ± 0.42	70.6 ± 0.52
	HV1	HV1	HV1	
24(not used)	67.2 ± 0.44	67.7 ± 0.75	71.6 ± 0.88	67.4 ± 0.67
36	63.0 ± 0.30	63.2 ± 0.39	68.5 ± 0.82	68.1 ± 0.72
48	61.4 ± 0.82	63.7 ± 0.26	64.3 ± 0.67	62.4 ± 0.40
60	57.7 ± 0.54	60.8 ± 0.59	61.9 ± 0.66	61.8 ± 0.39
72	58.6 ± 0.50	57.8 ± 0.25	61.8 ± 0.55	59.6 ± 0.52
100	55.3 ± 0.30	58.1 ± 0.62	58.2 ± 0.42	57.8 ± 0.70

Table C.2: ***Measured hardness for other KK alloys during over-ageing at 250°C.***

Time (h)	**KK1** HV5	**KK13** HV5	**KK24** HV5
0.00	124.9 ± 1.06	121.1 ± 0.74	106.9 ± 0.80
0.25	109.5 ± 0.81	105.8 ± 0.65	95.0 ± 0.67
0.50	107.3 ± 0.92	104.0 ± 0.30	94.0 ± 0.60
1.00	103.1 ± 0.96	99.2 ± 0.33	90.8 ± 0.36
1.50	100.1 ± 1.07	97.0 ± 0.54	89.3 ± 0.58
2.00	94.7 ± 0.52	95.2 ± 0.61	85.9 ± 0.48
2.50	95.5 ± 0.98	92.6 ± 0.34	85.4 ± 0.85
3	96.1 ± 0.84	92.8 ± 0.53	87.3 ± 0.21
4	93.1 ± 0.90	91.0 ± 0.26	84.7 ± 0.67
5	91.7 ± 0.63	88.9 ± 0.55	83.0 ± 0.65
7	88.9 ± 0.77	85.8 ± 0.25	81.3 ± 0.33
10	84.3 ± 0.30	83.4 ± 0.40	78.6 ± 0.64
15	81.7 ± 0.60	82.2 ± 0.20	77.5 ± 0.43
24	77.3 ± 0.67	76.5 ± 0.31	73.4 ± 0.31
	HV1	HV1	HV1
24(not used)	74.2 ± 0.77	76.2 ± 0.53	71.5 ± 0.52
36	71.9 ± 0.57	74.3 ± 0.56	68.7 ± 0.37
48	67.7 ± 0.79	68.5 ± 0.54	67.0 ± 0.56
60	62.6 ± 0.45	65.9 ± 0.41	63.2 ± 0.76
72	64.2 ± 1.13	61.1 ± 0.43	61.5 ± 0.48
100	59.6 ± 0.76	57.1 ± 0.31	56.9 ± 0.62

Table C.3: ***Measured hardness during over-ageing at 250°C for the 100h samples used for TEM specimen preparation.***

Time (h)	**KK30** HV5	**KK31** HV5	**KK32** HV5	**KK33** HV5
T6	109.7 ± 0.52	113.6 ± 0.45	118.9 ± 0.87	118.9 ± 0.77
	HV1	HV1	HV1	HV1
100h	56.6 ± 0.58	59.0 ± 0.49	60.1 ± 0.41	60.3 ± 0.45

Table C.4: ***Measured hardness during over-ageing at 250°C. Tested at Hydro Aluminium in Sunndalsøra.***

Time (h)	**KK13** HV5	**KK30** HV5
T6	117.0 ± 0.30	110.7 ± 0.76
0.5	104.8 ± 0.29	97.1 ± 0.62
3	95.1 ± 0.46	88.6 ± 0.54
15	83.3 ± 0.21	78.3 ± 0.37

Table C.5: ***Measured hardness during over-ageing at 220°C.***

Time (h)	**KK13** HV5
0.00	117.8 ± 0.36
0.25	112.4 ± 0.40
0.50	112.9 ± 0.69
1.00	111.5 ± 0.52
1.50	110.6 ± 0.65
2.00	109.6 ± 0.45
24.00	100.0 ± 0.21
100.00	86.7 ± 0.33

Appendix D

TEM Pictures

These are the images taken on the CM30 and were used in the microstructure determination in Chapter 4.

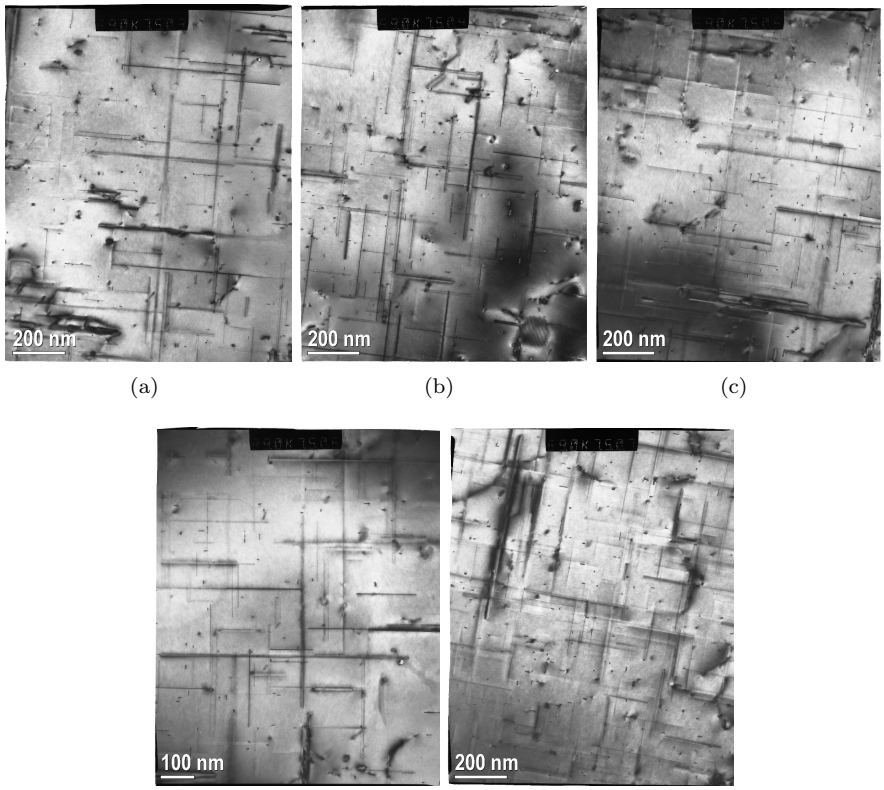

Figure D.1: ***The TEM images of KK30 after 24 hours at 250°C used for counting precipitates and measuring lengths.***

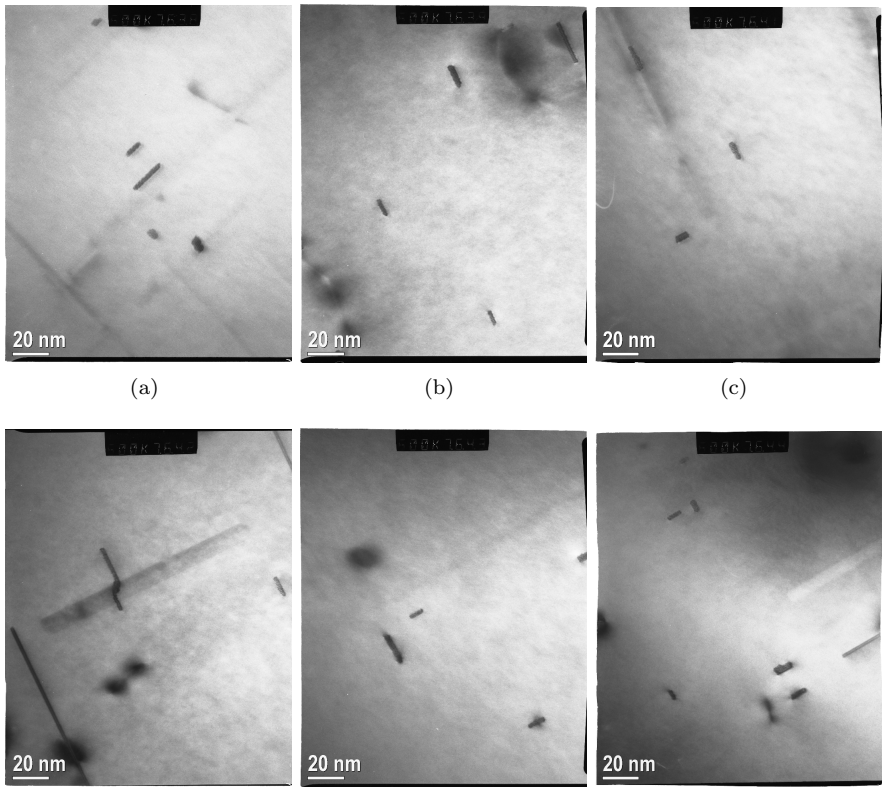

(a) (b) (c)

(d) (e) (f)

Figure D.2: ***The TEM images of KK30 after 24 hours at 250°C used for measuring cross sections.***

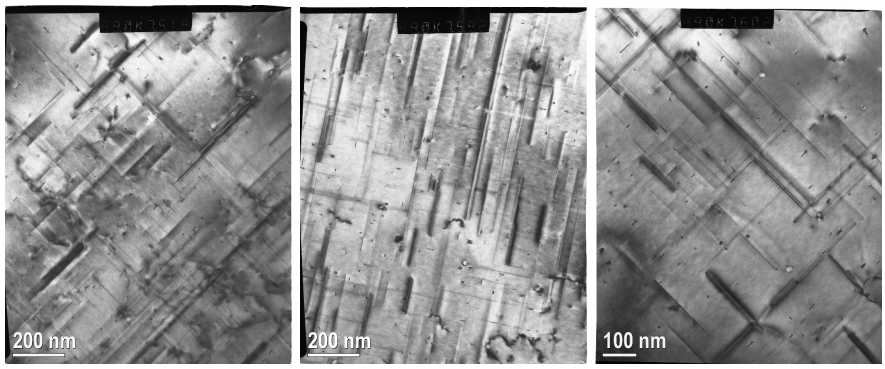

Figure D.3: ***The TEM images of KK33 after 24 hours at 250°C used for counting precipitates and measuring lengths.***

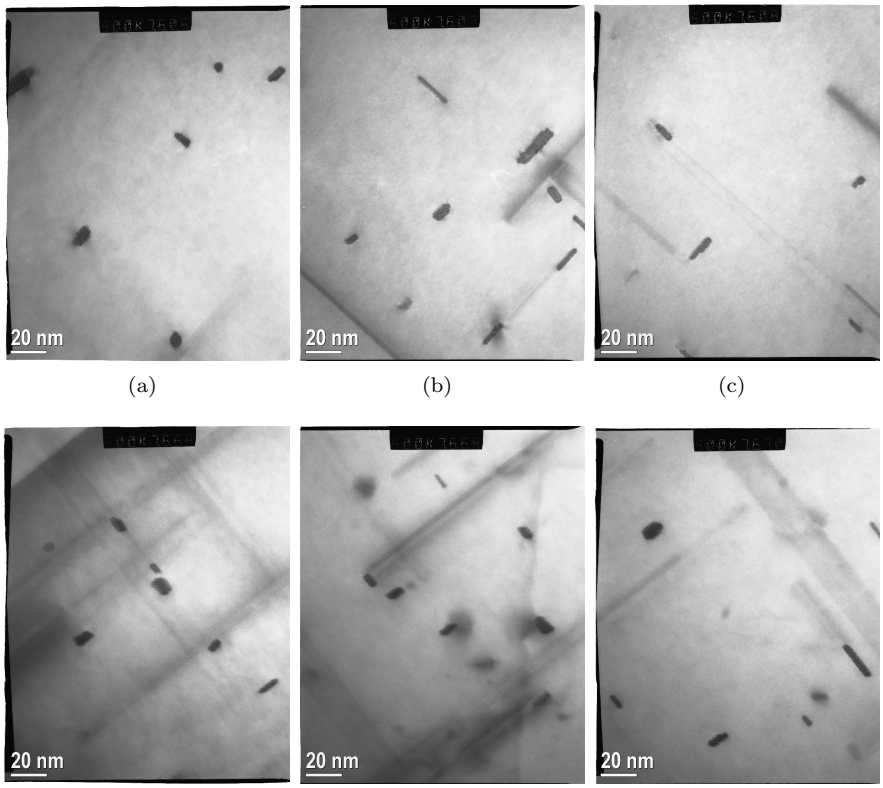

(a) (b) (c)

(d) (e) (f)

Figure D.4: ***The TEM images of KK33 after 24 hours at 250°C used for measuring cross sections.***

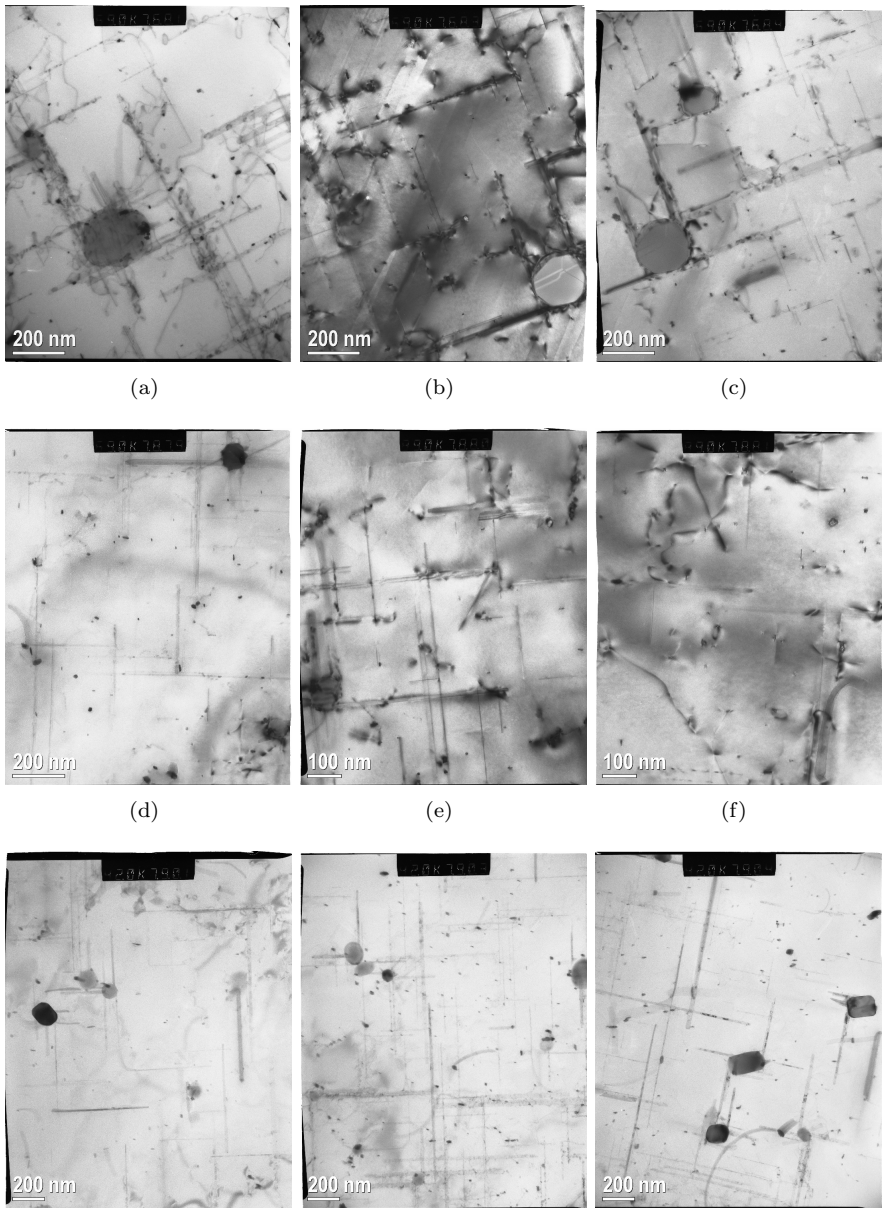

Figure D.5: ***The TEM images of KK30 after 100 hours at 250°C. (a)–(f) was used for counting precipitates, and all were used for measuring lengths.***

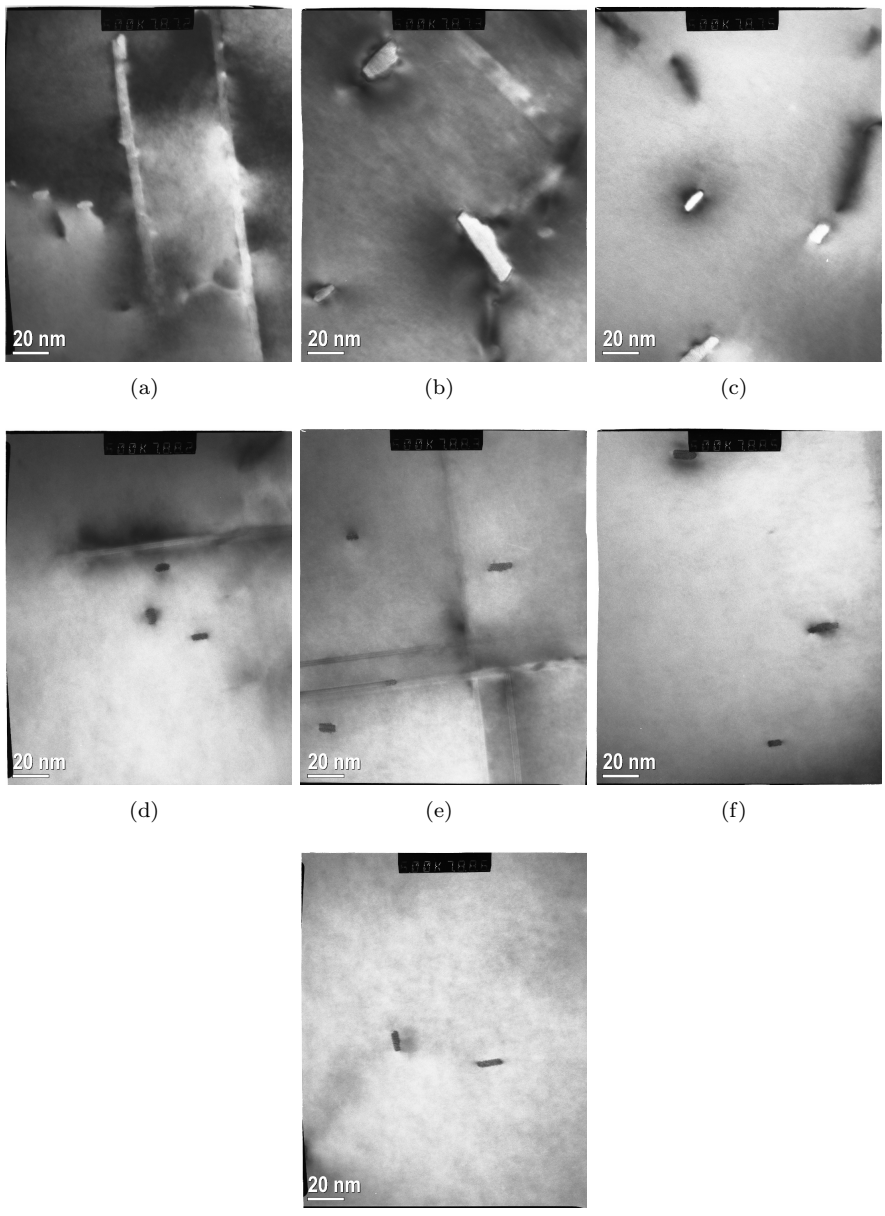

(a) (b) (c)

(d) (e) (f)

(g)

Figure D.6: ***The TEM images of KK30 after 100 hours at 250°C used for measuring cross sections.***

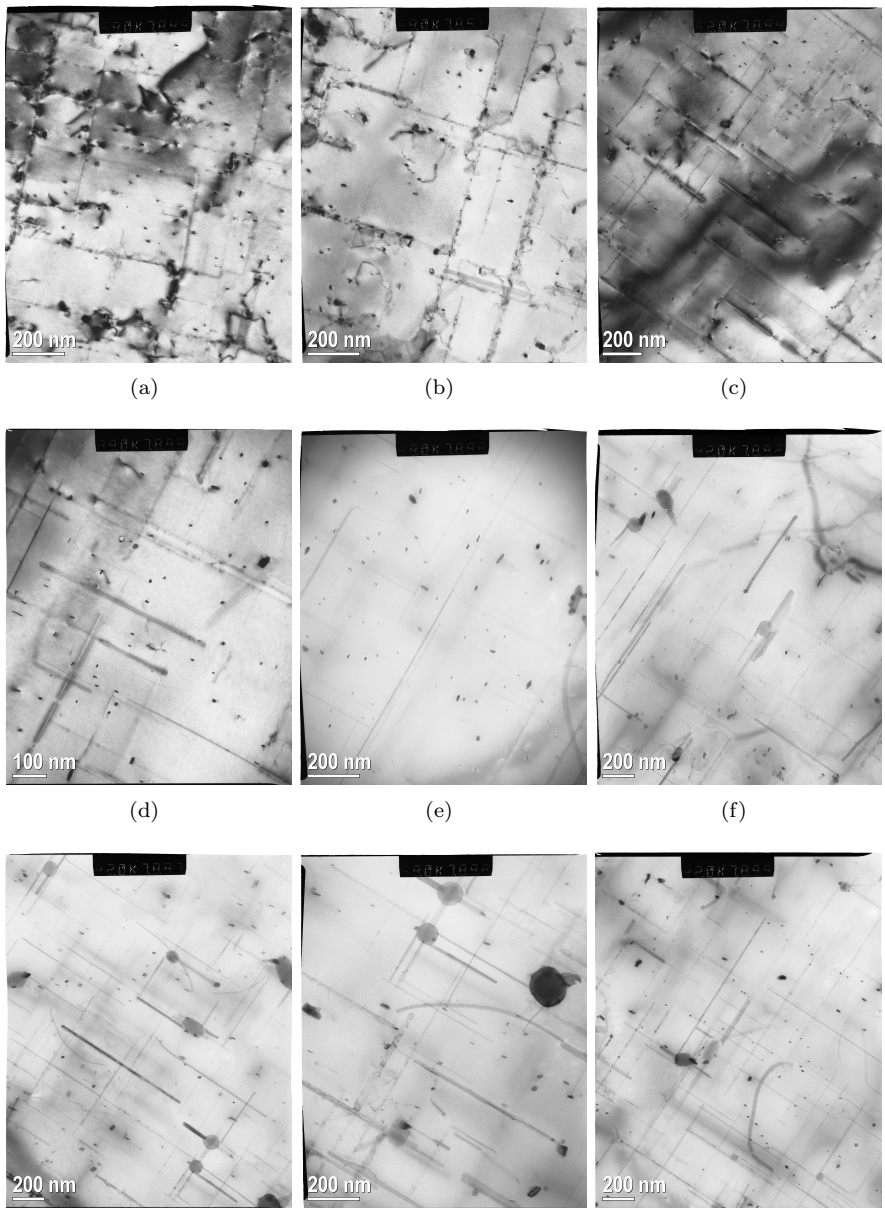

Figure D.7: ***The TEM images of KK33 after 100 hours at 250°C. (a)–(e) was used for counting precipitates, and (c)–(i) were used for measuring lengths.***

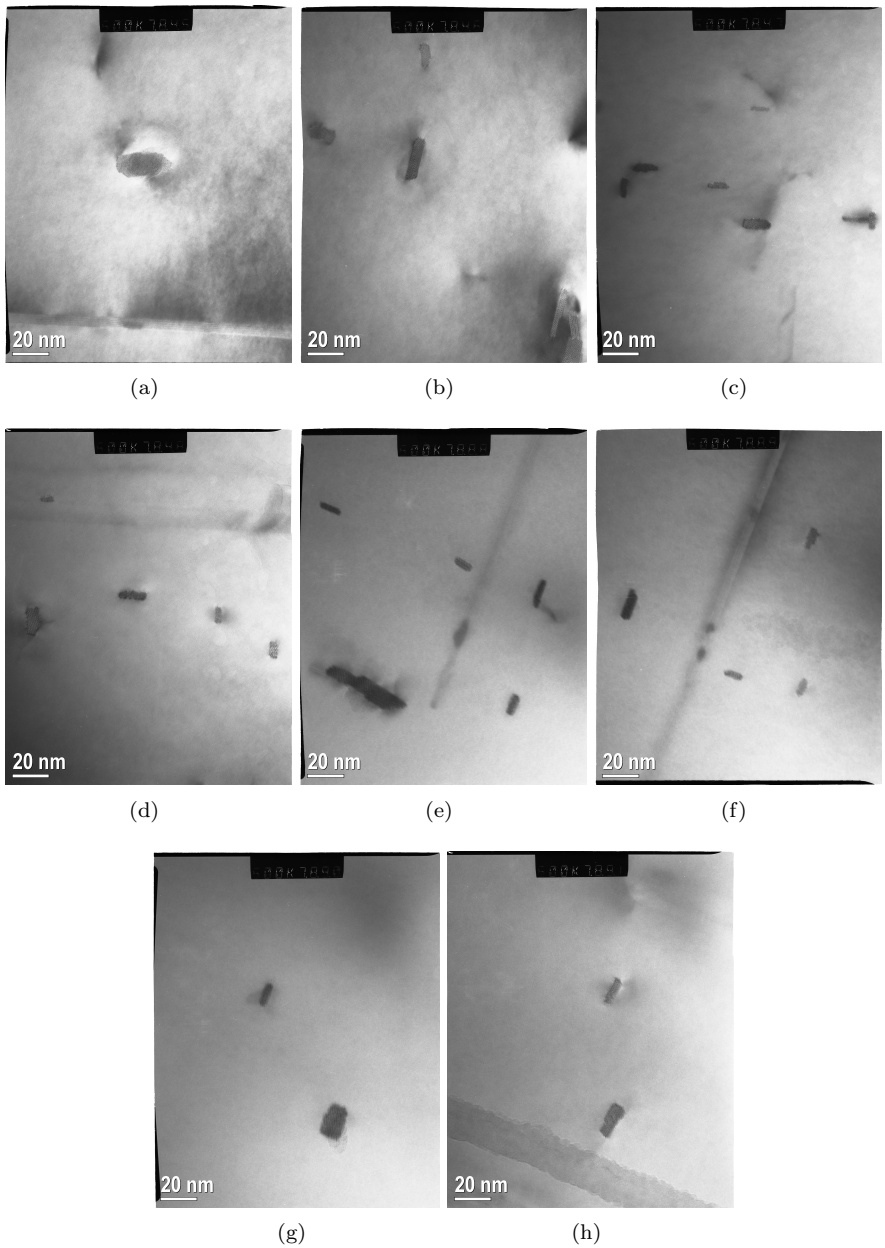

(a) (b) (c)

(d) (e) (f)

(g) (h)

Figure D.8: ***The TEM images of KK33 after 100 hours at 250°C used for measuring cross sections.***

Bibliography

[1] William B. Frank, Warren E. Haupin, Helmut Vogt, et al. *Aluminum.* Wiley-VCH Verlag, 2000. Ullmann's Encyclopedia of Industrial Chemistry.

[2] Nærings og handelsdepartementet. Metallindustrien. `www.regjeringen.no/nb/dep/nhd/tema/norsk-naringsliv/metall.html`.

[3] Norsk Hydro ASA. `www.hydro.com`.

[4] Jan Fredrik Helgaker. High temperature stability of Al-Mg-Si-Cu alloys. Project work, NTNU, 2010.

[5] J. R. Davis & Associates. *Aluminum and Aluminum Alloys.* ASM International, 1993.

[6] aluMATTER. Materials Science & Engineering. `aluminium.matter.org.uk`.

[7] Calm Aluminium. Aluminium-Alloys. `www.calm-aluminium.com.au/Documents/Aluminium-Alloys.pdf`.

[8] William D. Callister and David G. Rethwisch. *Material Science and Engineering.* Wiley, 2011.

[9] C.D Marioara, S.J Andersen, J Jansen, and H.W Zandbergen. The influence of temperature and storage time at RT on nucleation of the β'' phase in a 6082 Al–Mg–Si alloy. *Acta Materialia*, 51(3):789 – 796, 2003.

[10] Charles Kittel. *Introduction to Solid State Physics.* John Wiley & Sons, 2005.

[11] David A. Porter, Kenneth E. Easterling, and Mohamed Y. Sherif. *Phase Transformations in Metals and Alloys.* CRC Press, 2008.

[12] John D. Verhoeven. *Fundamentals of Physical Metallurgy.* John Wiley & Sons, 1975.

[13] C. D. Marioara, S. J. Andersen, H. W. Zandbergen, and R. Holmestad. The influence of Alloy Composition on Precipitates in the Al-Mg-Si System. *Metallurgical and Materials Transactions A*, 36(3):691–702, 2005.

[14] R. Vissers, M. A. van Huis, J. Jansen, et al. The crystal structure of the β' phase in Al-Mg-Si alloys. *Acta Materialia*, 55(11):3815–3823, 2007.

[15] S.J. Andersen, H.W. Zandbergen, J. Jansen, et al. The crystal structure of the β'' phase in Al–Mg–Si alloys. *Acta Materialia*, 46(9):3283 – 3298, 1998.

[16] C.D. Marioara, S.J. Andersen, T.N. Stene, et al. The effect of Cu on precipitation in Al-Mg-Si alloys. *Philosophical Magazine*, 87(23):3385–3413, 2007.

[17] C.D. Marioara, S.J. Andersen, J. Jansen, and H.W. Zandbergen. Atomic model for GP-zones in a 6082 Al–Mg–Si system. *Acta Materialia*, 49(2):321 – 328, 2001.

[18] D.J Chakrabartia and David E Laughlin. Phase relations and precipitation in Al–Mg–Si alloys with Cu additions. *Progress in Materials Science*, 49(3-4):389–410, 2004.

[19] C. Ravi and C. Wolverton. First-principles study of crystal structure and stability of Al–Mg–Si–(Cu) precipitates. *Acta Materialia*, 52(14):4213–4227, 2004.

[20] Ruben Bjørge. *Scanning transmission electron microscopy studies of precipitation in Al-Mg-Ge alloys*. PhD thesis, NTNU, 2011.

[21] Nobelprize.org. The Transmission Electron Microscope. `www.nobelprize.org/educational/physics/microscopes/tem/`.

[22] David B. Williams and C. Barry Carter. *Transmission Electron Microscopy*. Springer, 2009.

[23] Sigurd Wenner. PhD. student, NTNU. Private communications.

[24] Calin D. Marioara and Sigmund J. Andersen. Methodology for microstructure quantification in 6xxx aluminium alloys, 2009. Memo.

[25] Calin D. Marioara. SINTEF Materials and Chemistry. Private communications.

[26] Norsk Hydro ASA. High temperature stable aluminium alloy, 2011. Patent. PCT/NO2011/000111.

[27] Amund F. Utne. High Temperature Stability Tests of KK Alloys. Project work, NTNU, 2011.

[28] Jon Holmestad. High-Temperature Stability of Al-Mg-Si-Cu Alloys. Project work, NTNU, 2008.

[29] Jon Holmestad. PhD student, NTNU. Private communications.

[30] RUSAL. All About Aluminum. `www.aluminiumleader.com/en/`.

[31] ETH Zürich. Electron Microscopy. `www.microscopy.ethz.ch`.